

Remote Sensing of Chemical Thinning

Russell Main, Mark Jayson B. Felix, Michael S. Watt and Robin J.L. Hartley



Date: 06 June 2025

Report No: PSP-T036

Funded by:

Ministry for Primary Industries
Manatū Ahu Matua



supported by
forestgrowers
commodity levy

TABLE OF CONTENTS

Remote Sensing of Chemical Thinning	1
EXECUTIVE SUMMARY	1
INTRODUCTION	2
METHODS.....	3
Study Site	3
Methods Overview	4
Data Collection.....	4
Experimental Design and Implementation	4
Visual Assessment Data Collection	5
Remote Sensing Datasets.....	6
Data Analysis and statistical methods	10
Visual Assessments	10
Spectral Data	10
Classification of <i>Cull</i> and <i>Crop</i> Trees	10
Sensor Simulation: Exploring Cost-Effective Monitoring	11
RESULTS	12
Ground Observations and Visual Assessments.....	12
Treatment Differences in Multispectral Data.....	13
Treatment Differences in Hyperspectral Data.....	15
Classification of <i>Cull</i> from <i>Crop</i> Trees	17
Classification Results using Multispectral Data.....	17
Classification Results using Hyperspectral Data.....	18
Sensor Simulation Results	18
DISCUSSION AND CONCLUSIONS	19
ACKNOWLEDGEMENTS	22
REFERENCES	23
APPENDICES.....	35

Disclaimer

This report has been prepared by Scion Research for Forest Growers Research Ltd (FGR) subject to the terms and conditions of a research fund agreement dated March 2022.

The opinions and information provided in this report have been provided in good faith and on the basis that every endeavour has been made to be accurate and not misleading and to exercise reasonable care, skill and judgement in providing such opinions and information.

Under the terms of the Services Agreement, Scion Research liability to FGR in relation to the services provided to produce this report is limited to the value of those services. Neither Scion nor any of its employees, contractors, agents or other persons acting on its behalf or under its control accept any responsibility to any person or organisation in respect of any information or opinion provided in this report in excess of that amount.

EXECUTIVE SUMMARY

Chemical thinning is attracting increasing interest among New Zealand forest managers as a cost-effective and safer alternative to traditional thinning methods, particularly in steep or inaccessible terrain. This study investigated the potential for unmanned aerial vehicles (UAVs) equipped with hyperspectral and multispectral sensors to detect early herbicide-induced stress in radiata pine (*Pinus radiata*), in support of efforts to improve quality control and monitoring in chemical thinning operations.

The research was carried out in a nine-year-old radiata pine stand using a staggered herbicide treatment design, where subsets of trees were treated over a six-week period with Metsulfuron-methyl. A single UAV imaging campaign was timed to capture a time series of canopy responses across treated and untreated trees, with the treated group spanning 13 to 47 days after treatment (DAT). Visual assessments were conducted in parallel to confirm the timing of symptom development.

The study found that UAV-based spectral imaging was able to detect stress responses before significant visual discolouration was observed, which began around 25 DAT. Classification models based on narrow-band hyperspectral indices achieved robust separation of treated and untreated trees as early as 13 DAT, with F1 scores reaching 0.74. Multispectral models showed comparable performance from 18 DAT onward (F1 score = 0.77). Across both sensor types, pigment-sensitive vegetation indices, particularly variants of the Photochemical Reflectance Index (PRI), emerged as consistent top predictors.

To evaluate the potential for wider operational uptake, a simulation exercise was conducted using the hyperspectral dataset to reproduce the band configurations of lower-cost, commercially available multispectral sensors (4–5 bands, \$10–15k). These simulated sensors (e.g. DJI Phantom 4 (Multispectral) and DJI Mavic 3M) achieved high classification accuracy from 27 DAT onward, with F1 scores reaching 0.92 by 47 DAT. This performance closely matched that of the more expensive 10-band research-grade multispectral system and approached that of the hyperspectral model for certain time periods, despite their more limited spectral resolution.

These findings provide operational insight into the early detection window for herbicide-induced stress, suggesting a baseline of 13 to 18 days after treatment as a target for remote monitoring. The performance of low-cost multispectral PRI indices also supports their potential for routine implementation.

The work contributes to the growing body of research supporting remote sensing applications in precision forestry and in several ways offer a foundation for the development of scalable tools to support chemical thinning practices across New Zealand.

This report summarises, and adds to, work that has been published in a peer review journal:

Main, R., Felix, M. J. B., Watt, M. S., & Hartley, R. J. L. (2025). Early Detection of Herbicide-Induced Tree Stress Using UAV-Based Multispectral and Hyperspectral Imagery. Forests, 16(8), Article 8.
<https://doi.org/10.3390/f16081240>

INTRODUCTION

Thinning is an important forest management practice used to reduce tree density and improve the growth, health, and resilience of remaining *crop* trees (Martín-Benito et al., 2010). In areas where it is impractical or uneconomical to extract thinned trees, they are often cut and left to decompose on site. This is commonly referred to as thinning to waste (Willoughby et al., 2017). While chainsaw-based thinning has traditionally been the standard approach in New Zealand, chemical thinning has been explored since the 1960s as a potential alternative (Beveridge & Hedderwick, 1962; Maclaren et al., 1999; Tustin, 1969). Advances in herbicide formulations and application methods have led to renewed interest in this practice, offering potential benefits such as reduced chainsaw-related injuries, lower operational costs, and improved stand stability following wind events (Maclaren et al., 1999; Tubby et al., 2017; Willoughby et al., 2017). Chemical thinning also presents a safer and more cost-effective solution for managing stands in steep or remote areas where manual thinning is less feasible (Holt & Dickinson, 2024).

Chemical thinning relies on the use of herbicides that induce physiological stress in trees by disrupting key metabolic pathways. These disruptions result in changes to leaf structure and biochemistry, including variations in pigment, water, and nitrogen content (Sherwani et al., 2015; Scholten et al., 2019). Such changes affect how leaves interact with light, altering reflectance and absorption characteristics across different wavelengths (Blackburn, 1999). Relationships between spectral reflectance and foliar biochemistry, particularly pigments associated with photosynthesis, have been widely established (Blackburn, 2007; Zhang et al., 2020; Sanaeifar et al., 2023), with the visible and near-infrared (VNIR) regions of the spectrum shown to be particularly sensitive to stress-induced pigment variation (Vogelmann et al., 1993; Carter & Miller, 1994; Coops et al., 2003; Behmann et al., 2014).

Remote sensing technologies, particularly UAVs equipped with multispectral and hyperspectral imaging sensors that capture information in these spectral regions, have become valuable tools for monitoring tree stress from both biotic and abiotic sources (Behmann et al., 2014; Lausch et al., 2016; Adão et al., 2017; Oerke, 2020; Le et al., 2023). Hyperspectral sensors collect reflectance data across hundreds of narrow, contiguous spectral bands spanning the visible, near-infrared, and shortwave infrared regions (Goetz et al., 1985). Derived indices, such as narrow-band hyperspectral indices (NBHIs), have been effectively used to detect disease-related stress in both laboratory (Watt, Bartlett, et al., 2023; Watt et al., 2024) and field-based forestry studies (Zarco-Tejada et al., 2018; Watt, Poblete, et al., 2023). Abiotic stress detection, including drought (Kim et al., 2011; Buddenbaum et al., 2015; Watt et al., 2021; Felix et al., 2025), fertiliser application (Watt et al., 2019, 2020), and herbicide response (Scholten et al., 2019), has also been demonstrated using hyperspectral methods.

Although hyperspectral imaging offers higher spectral resolution, UAV-based multispectral sensors remain popular for operational use due to their lower cost and ease of deployment. These sensors have been widely applied to detect tree stress associated with pests, disease, drought, fire, and waterlogging (Ecke et al., 2022). One relevant study by Dash et al. (2017) simulated disease-like stress in mature radiata pine using herbicide treatments and monitored the physiological response over time with multispectral UAV imagery. Their results showed that early-stage stress could be detected using red-edge and near-infrared spectral regions, highlighting the value of high-resolution UAV imagery for forest health monitoring. However, the study also noted limitations in the sensor's sensitivity and suggested that more advanced systems could enhance early detection capabilities. Complementary findings from Scholten et al. (2019), who used hyperspectral imaging in a controlled tree trial, further support the potential for early identification of herbicide-induced stress.

As sensing technologies and analytical methods continue to improve, remote sensing is expected to play an increasingly important role in supporting precision forestry. UAV-based imaging offers a flexible and cost-efficient method for repeatedly collecting high-resolution data that can support proactive monitoring of tree stress across operational forestry sites (Lassalle, 2021; Ecke et al., 2022; Pan et al., 2023; da Silva et al., 2024). Chemical thinning operations may benefit from the

early identification of treated trees, which could improve resource planning and treatment validation in challenging environments.

This project investigated whether UAV-based spectral imaging could be used to detect early signs of herbicide-induced stress in a chemically thinned radiata pine stand. By capturing data across a time series of staggered herbicide treatments, the aim was to determine how reliably treated trees could be distinguished from untreated ones prior to significant visual discolouration. The study sought to contribute to a growing body of research exploring the use of remote sensing for early detection of tree stress, and to address a recognised knowledge gap around field-based monitoring of herbicide effects in forestry. The work also potentially establishes a baseline for UAV-based monitoring of chemical thinning activities in New Zealand's forestry sector.

METHODS

Study Site

This trial was carried out in a ~6 ha section of a 78 ha radiata pine stand located in Omataroa Forest, Bay of Plenty, New Zealand (Figure 1). The site sits at around 213 meters above sea level on gently sloping terrain with well-drained pumice soils typical of the region. Weather during the trial (October 2024 to February 2025) was moderate, with 122 mm of total rainfall and an average temperature of 17.1°C. No signs of common diseases like red needle cast (*Phytophthora pluvialis*) or Dothistroma needle blight (*Dothistroma septosporum*) were observed prior to the trial.

The trees were planted in 2015 at 650 stems per hectare (sph). The site had not undergone any pruning, and this study focused on the first chemical thinning, initiated in 2024 when the stand was nine years old, with a target residual stocking of 450 sph. A representative sample of 100 trees recorded an average diameter at breast height (1.4 m) of 26.3 cm and an average height of 20 m.

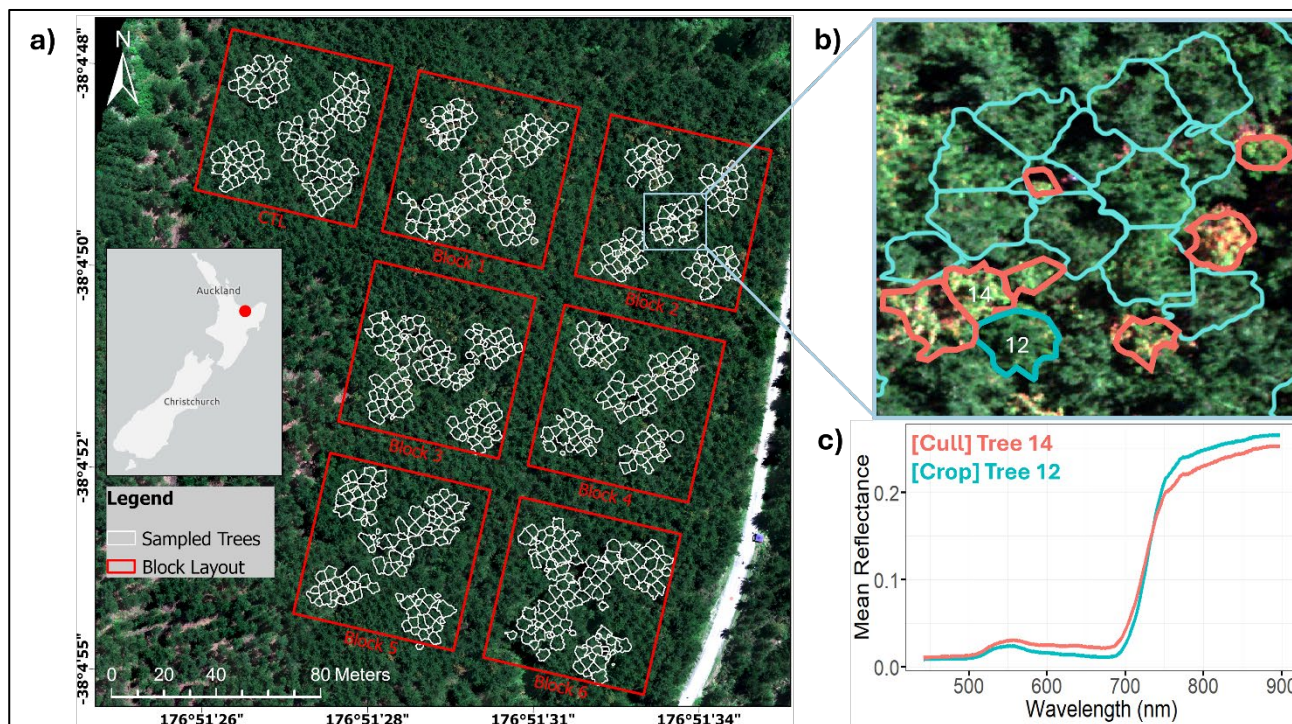


Figure 1: Overview of the study site, experimental design, and spectral variation. (a) UAV-derived true-colour orthomosaic showing six treatment blocks and a control (CTL) block, with sampled trees outlined. (b) Zoomed-in view of Block 2 with hyperspectral imagery and crown delineations (*cull* trees in red, *crop* in cyan). (c) Mean reflectance spectra of a selected *cull* and *crop* tree.

Methods Overview

We followed a four-step process to assess the herbicide stress in the trees (Figure 2). First, we set up seven treatment blocks, marked trees for herbicide application, and used UAV LiDAR and RGB imagery to link ground-identified trees with their canopy positions. Herbicide was applied in a staggered way across blocks, and we carried out three rounds of visual assessments using a six-class scale to track canopy discoloration. A single UAV flight, done 47 days after the first treatment and 13 days after the last, captured multispectral and hyperspectral imagery, allowing us to observe a range of stress stages in one dataset. The images were processed to correct for lighting, align the canopy, and extract reflectance and over 65 vegetation indices related to pigment, structure, water, and stress. Finally, we combined visual scores with statistical tests and used a machine learning model (SVM) to classify treated and untreated trees, with accuracy measured using precision, recall, and F1 score.

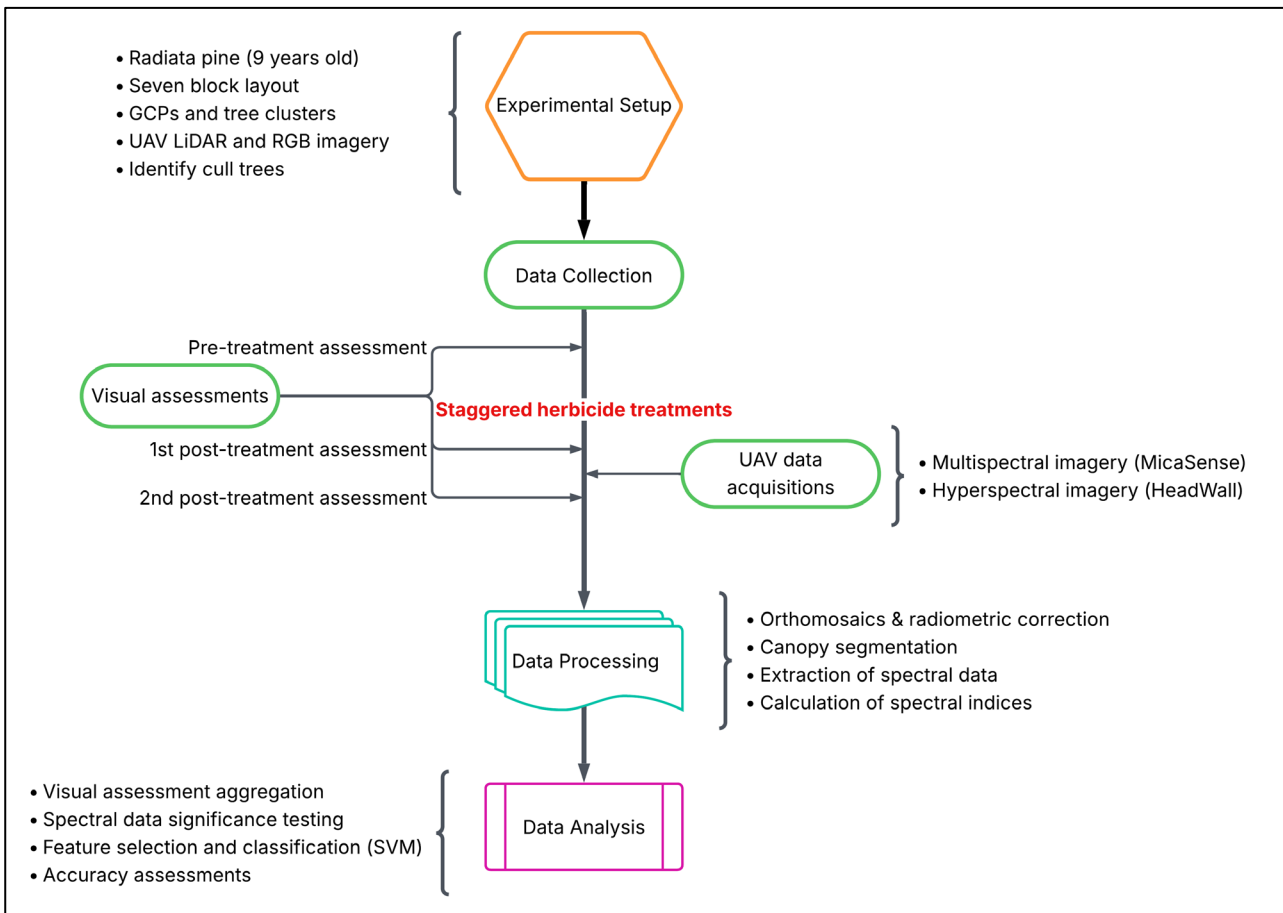


Figure 2: Overview of the experimental design and workflow. The study followed four stages: setup, data collection, processing, and analysis. Visual assessments and a single UAV flight captured multispectral and hyperspectral data across 13–47 Days After Treatment (DAT), enabled by a staggered treatment schedule. Processing included canopy segmentation, index calculation, and classification using Support Vector Machines (SVM).

Data Collection

Experimental Design and Implementation

The experiment was designed to mimic real-world thinning operations rather than follow a fully randomised layout. This approach improved UAV flight efficiency and helped ensure accurate matching of individual trees between field observations and image data. The trial was established across seven 0.4 ha blocks within a radiata pine stand (Figure 1). Six blocks were designated for herbicide treatment, while the seventh served as an untreated control. Each block contained five

clusters of approximately 20 trees. Within each cluster, an experienced thinning contractor identified and selected *cull* trees for treatment. Trees were selected based on typical operational thinning criteria, such as dominance, stem quality (including health, straightness, and branching), and spacing. These factors are commonly used to identify and retain the most desirable trees as the final crop. These (*cull*) trees were treated with Metsulfuron methyl, applied at a concentration of 20 grams per litre of water. A single 5 ml dose was administered via a drilled hole in each selected tree. The same dosage and application method were used for all treated trees, with no differences between blocks or individual trees. Remaining trees within each cluster were classified as *crop* trees.

Herbicide applications in the six treatment blocks were staggered over a 34-day period, with intervals of 5 to 9 days between treatments (Table 1). This phased approach helped reduce the number of required site visits and UAV flights, while enabling monitoring of foliage changes across a range of days after treatment (DAT). Three post-treatment assessments were conducted, each completed in a single day (Table 1): the first visual assessment on 13 December 2024 (11–45 DAT), UAV imagery acquisition on 15 December 2024 (13–47 DAT), and a second visual assessment on 24 January 2025 (53–87 DAT). Note that the control block was not treated, but trees were still designated as either *crop* or untreated *cull* and monitored throughout the study. This provided a reference to assess whether any changes in *crop* trees in the treated blocks were due to herbicide transfer. Consistent spectral and visual patterns between the control and treated *crop* trees would suggest minimal or no herbicide drift.

In total, 707 trees were marked, geolocated, and assessed visually across the seven blocks, with approximately 100 trees per block distributed around five centrally located plots (Figure 1). The overall *crop*-to-*cull* tree ratio was approximately 2.3:1, with 67–75 *crop* trees and 29–33 *cull* trees per block. To enable precise alignment between ground observations and aerial imagery, five high-contrast ground control points (GCPs) were installed at each plot centre. These GCPs, consisting of matte black and retro-reflective white panels, were georeferenced using an Arrow Gold RTK receiver (EOS Position Systems Inc., Quebec, Canada). Around each GCP, a minimum of 20 trees were uniquely tagged, and their distances and bearings recorded, ensuring accurate matching between field-based measurements and canopy features in aerial imagery.

Table 1: Timeline of activities conducted across the six treatment blocks, with the corresponding days after treatment (DAT) calculated relative to the first post-treatment visual assessment, the UAV captures, and the second post-treatment visual assessment.

Date	Activity	1 st visual on 13	UAV captures on	2 nd visual on
		Dec. 2024	15 Dec. 2024	24 Jan. 2025
Days after treatment (DAT)				
17 Oct. 2024	Pre-treatment Visual Assessment	-	-	-
-	Control Block	-	-	-
29 Oct. 2024	Block 1 Treatment	45	47	87
04 Nov. 2024	Block 2 Treatment	39	41	81
13 Nov. 2024	Block 3 Treatment	30	32	72
18 Nov. 2024	Block 4 Treatment	25	27	67
27 Nov. 2024	Block 5 Treatment	16	18	58
02 Dec. 2024	Block 6 Treatment	11	13	53

Visual Assessment Data Collection

Visual assessments of canopy discoloration were carried out for each marked tree at three key time points: (i) prior to any herbicide application, (ii) close to the time of UAV data collection, and (iii) at the end of the trial. Each tree was observed from two opposing angles by the same experienced assessor, who was trained in evaluating canopy health and disease symptoms. Symptom severity was classified into six categories based on the percentage of canopy affected and associated colour changes. Trees with 0% discoloration were classified as such and exhibited a generally shiny green canopy, <20% discoloration as light (dull green), 20–40% discoloration as moderate (dull green

to pale yellow), 40–60% discolouration as high (dull green to yellow), 60–80% discolouration as extreme (yellow to orange), and 80–100% as severe (orange to brown) (Figure 3).

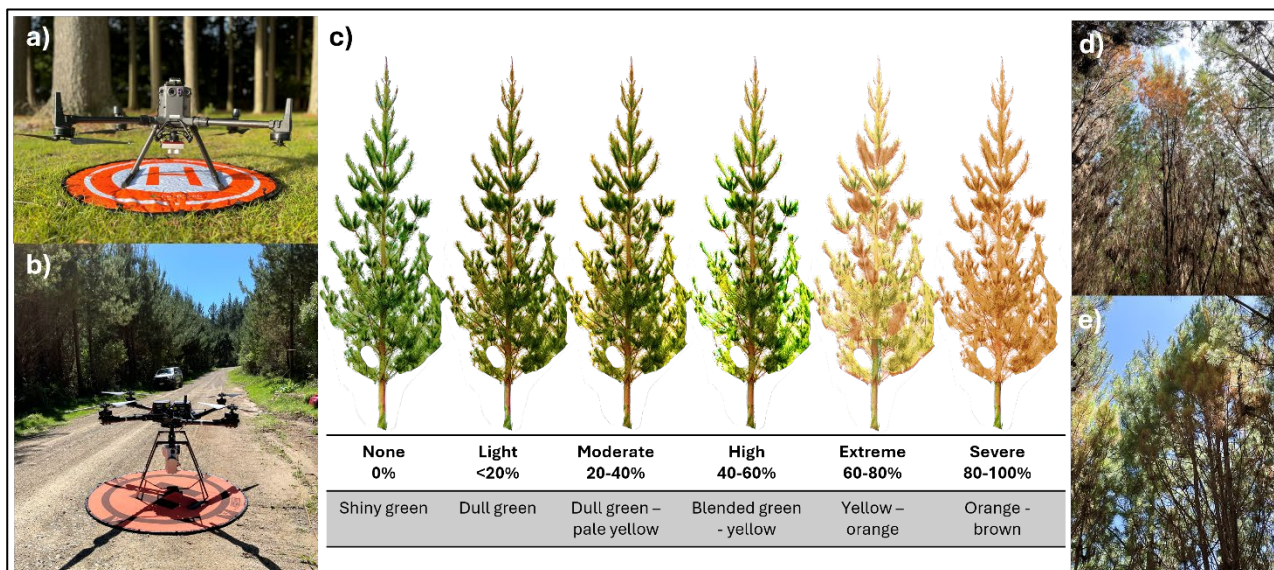


Figure 3: UAV and field assessment methodology. (a) DJI Matrice 300 UAV equipped with a MicaSense RedEdge sensor; (b) Freefly Alta-X equipped with the HeadWall hyperspectral sensor; (c) representation of the canopy discolouration categories ranging from healthy (shiny green) to severely discoloured (orange-brown); (d-e) ground-level views from within treatment plots showing variations in canopy discolouration.

Remote Sensing Datasets

A suite of UAV-mounted sensors was deployed to capture detailed spatial data across the treatment blocks, including light detection and ranging (LiDAR), high-resolution RGB imagery, and both multispectral and hyperspectral datasets.

- **LiDAR and RGB Data**

High-resolution RGB imagery was acquired both before and after the herbicide treatment, while LiDAR data were collected pre-treatment only, using DJI Zenmuse P1 and Zenmuse L1 sensors, respectively, mounted on a DJI Matrice 300 RTK platform (DJI, Shenzhen, China) (Figure 4). RGB imagery was captured from an altitude of 120 m at a flight speed of 5 m/s, with 85% forward and side overlap, yielding imagery at ~1.5 cm ground resolution. LiDAR data were collected using a grid-pattern flight path with 10 m spacing, flying at 3 m/s and 55 m altitude. The LiDAR system operated in repetitive scan mode at 160 Hz, recording up to three returns per pulse. To ensure spatial accuracy, the centres of high-contrast ground control points (GCPs), serving as plot centres within each treatment block, were extracted from the LiDAR point cloud and used to georeference the LiDAR and all subsequent image datasets.

LiDAR point clouds were pre-processed using LASTools (Version 2.0.3), including noise filtering, ground classification, digital terrain model (DTM) creation, and ground normalisation. A 25 cm resolution, pit-free canopy height model (CHM) was generated and smoothed with a 3 × 3 pixel moving window. Individual tree peaks were identified using a fixed 3 m local maxima algorithm, reflecting planting density. Tree peaks were verified against the high-resolution RGB imagery, and individual tree crowns were delineated using the (mcws) watershed segmentation algorithm from the ForestTools R package. Final crown polygons were manually inspected and adjusted to correct any misclassifications.

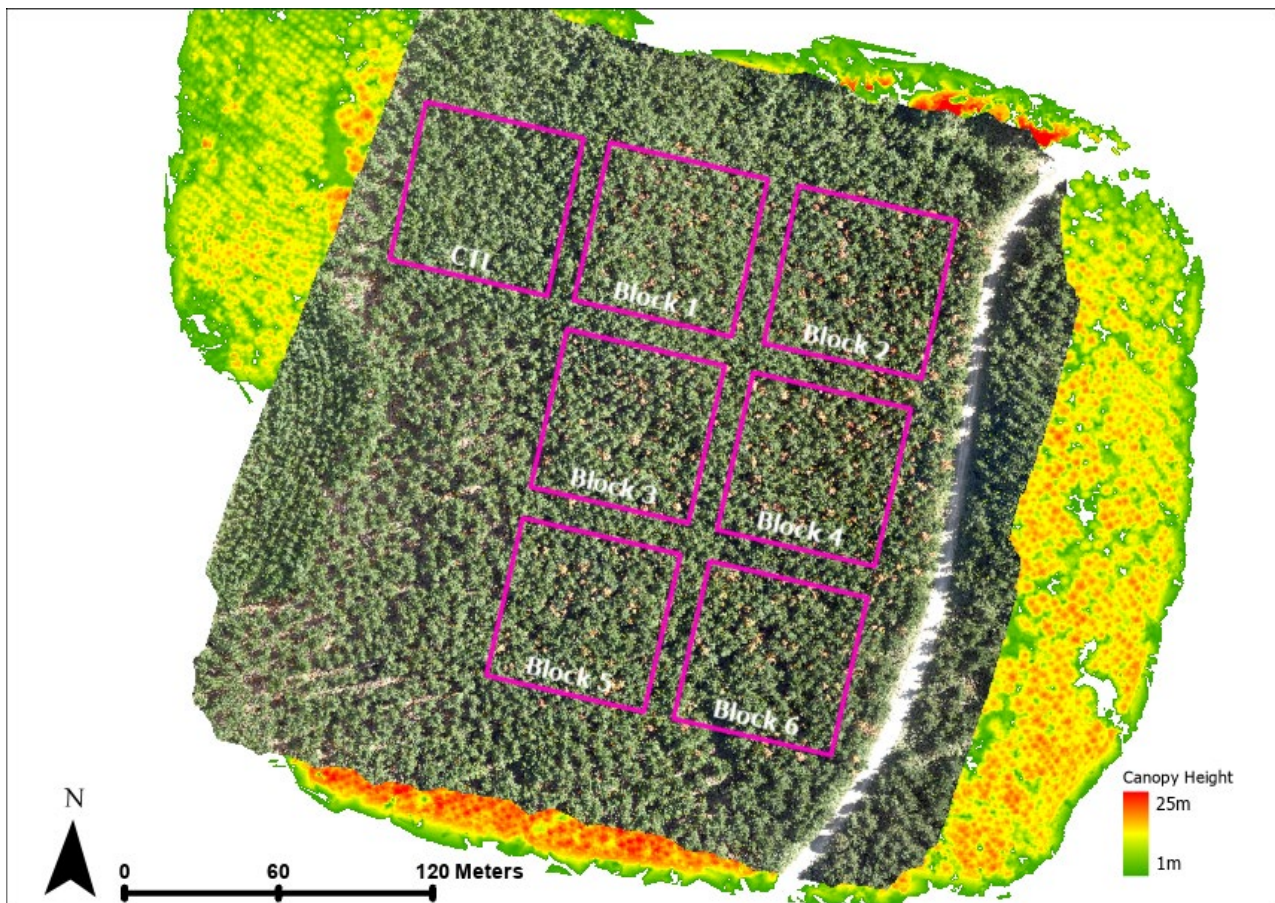


Figure 4: UAV-captured RGB imagery 87 days after treatment (DAT), overlaid on a LiDAR-derived canopy height model from the start of the experiment. Pink outlines show the treatment blocks (Blocks 1–6) and the untreated control (CTL). Canopy height ranges from 1 to 25 meters, with warmer colours indicating taller vegetation.

- **Multispectral Data**

Multispectral imagery was captured on 15 December 2024 using the MicaSense MX-Duo system (MicaSense Inc., Seattle, WA, USA) mounted on the DJI Matrice 300 RTK platform (Figure 5). This dual-camera system, comprising the RedEdge-MX and RedEdge-MX Blue sensors, captured ten discrete spectral bands: coastal blue (430–458 nm), blue (459–491 nm), two green bands (524–538 nm, 546–573 nm), two red bands (642–658 nm, 661–675 nm), three red-edge bands (700–710 nm, 711–723 nm, 731–749 nm), and near-infrared (813–870 nm).

Flight operations were conducted around midday under stable lighting conditions, with calibration performed using the MicaSense reflectance panel. Flights were conducted at 100 m altitude and 4.5 m/s speed, maintaining 90% forward and 85% side overlap. Imagery was processed and mosaicked using the open source photogrammetry software OpenDroneMap (v3.5.4), resulting in a georeferenced ~6 cm resolution mosaic aligned to the NZTM2000 coordinate system, with refinement against high-resolution RGB imagery and GCPs.

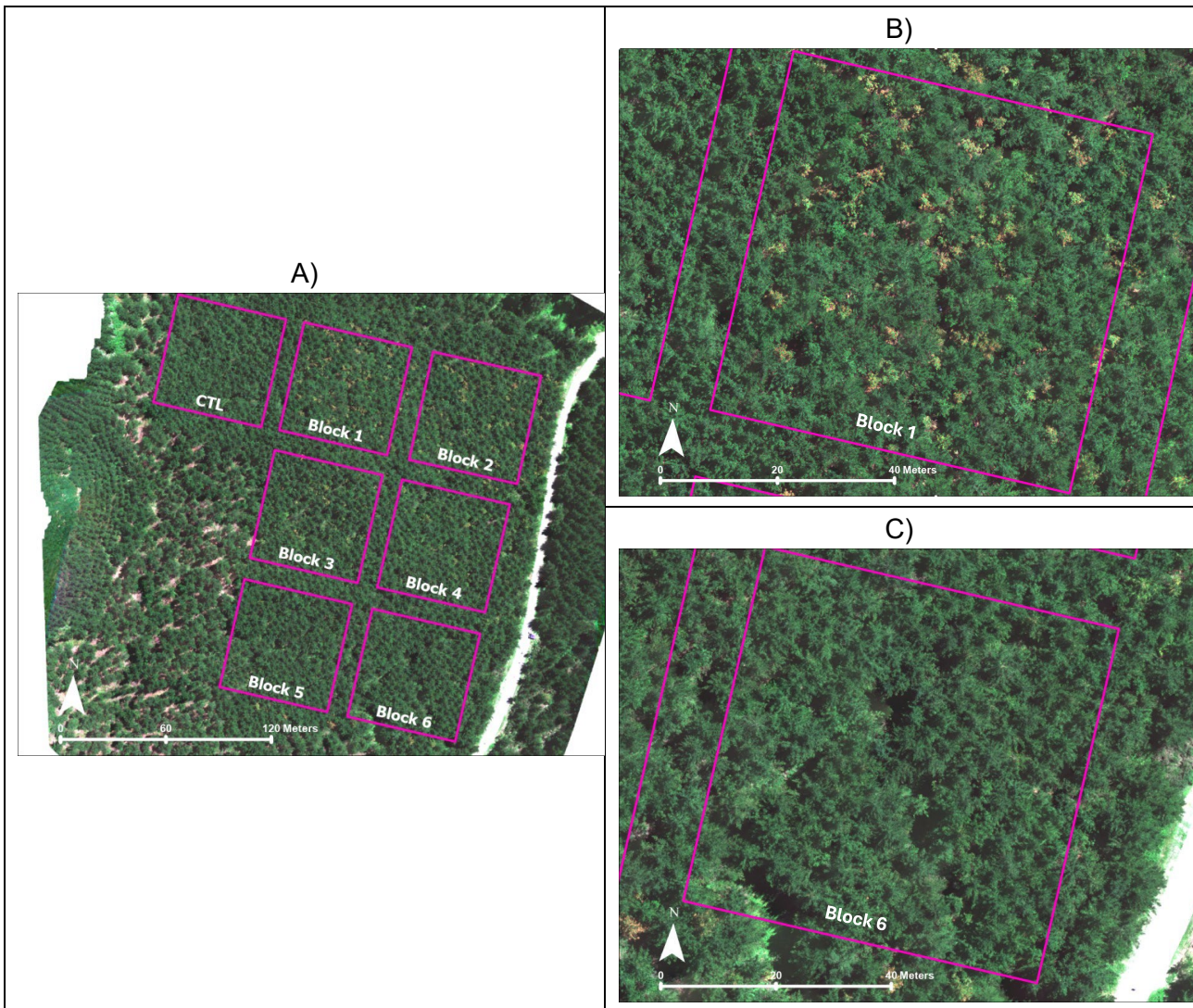


Figure 5: UAV-based multispectral imagery captured 47 days after treatment (DAT), showing all treatment blocks (A), with zoomed-in views of Block 1 (B) and Block 6 (C). Block 1 (45 DAT) shows visible canopy discoloration, while Block 6 (13 DAT) exhibits little to no discoloration.

- **Hyperspectral Data**

On the same date, hyperspectral imagery was collected using a Headwall Photonics VNIR sensor (Headwall Photonics Inc., Bolton, MA, USA) mounted on a Freely Alta-X UAV (Freely Systems Inc., Woodinville, WA, USA) (Figure 6). The sensor featured a 12 mm focal length and a 22.3° field of view, recording 273 narrow spectral bands between 400–1000 nm at 6 nm FWHM. Calibrated for midday radiance conditions via the HyperSpec® III software, the system captured data at 125 fps with an 8 ms integration time. Flights were conducted at 100 m altitude and 7.5 m/s speed, with 40% image overlap, following pre-programmed paths using UgCS flight planning software (SPH Engineering, Riga, Latvia).

Hyperspectral data processing was carried out using SpectralView®. Raw digital numbers were converted to radiance using sensor-specific calibration files and dark frame correction. Reflectance was calculated using a linear regression between measured radiance and a 56% grayscale calibration target. Orthorectification was applied to correct for geometric distortions using post-processed RTK data and LiDAR-derived DEMs, with further refinement through alignment with high-resolution RGB imagery and GCPs. The final hyperspectral reflectance cubes were georeferenced to NZTM2000 and achieved a spatial resolution of approximately 6 cm.

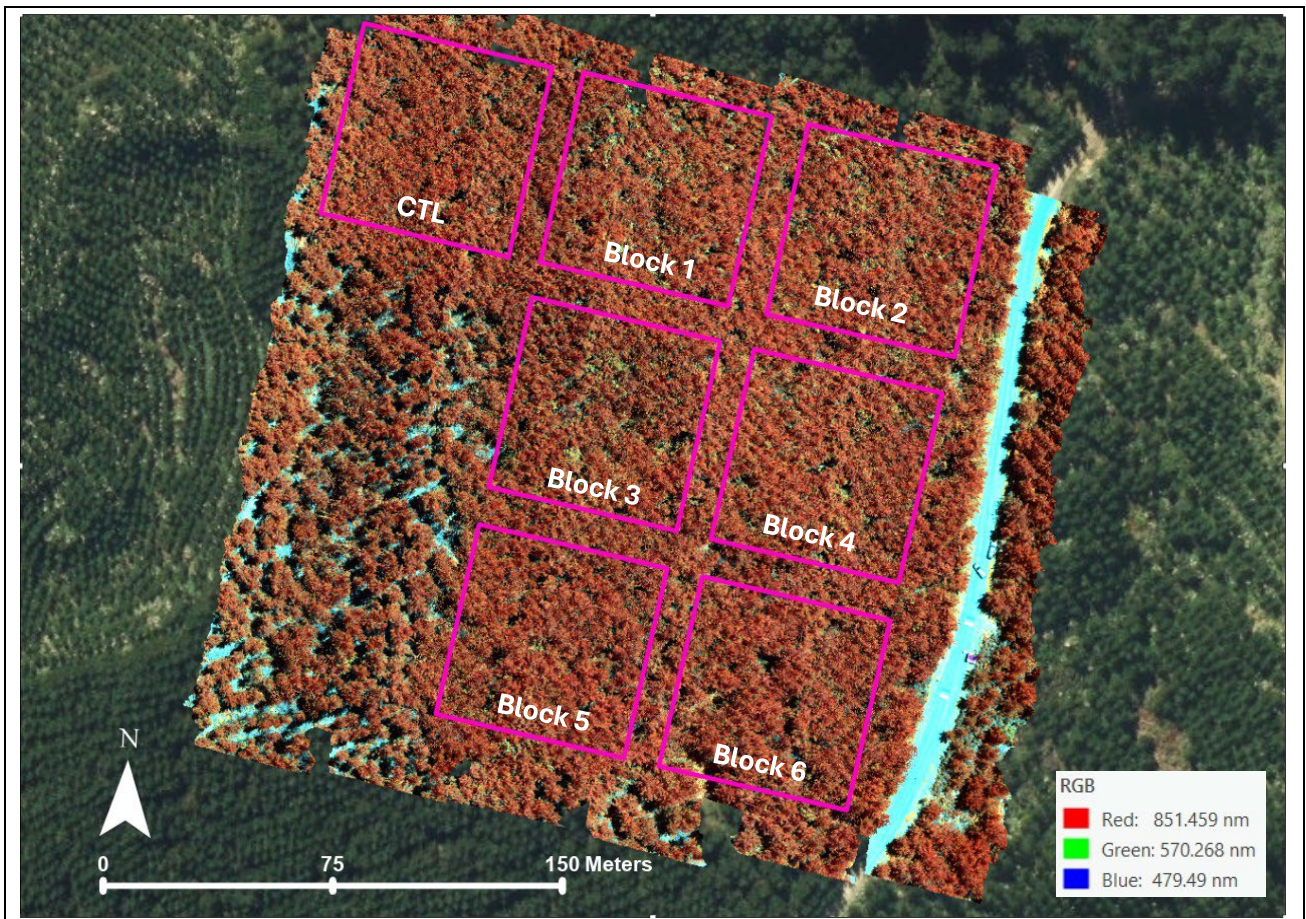


Figure 6: False-colour composite image from UAV-based hyperpectral data, using near-infrared (851 nm), green (570 nm), and blue (479 nm) bands. Treatment blocks (Blocks 1–6) and the untreated control (CTL) are outlined in pink.

Data Analysis and statistical methods

Visual Assessments

Discolouration scores from the three visual assessments served as ground-truth references for evaluating the onset and severity of herbicide-induced stress in treated trees. The proportion of trees within each discolouration class was calculated and visualised for both *crop* and *cull* treatments across all treatment blocks. These assessments were instrumental in identifying the timepoints when visible stress symptoms first emerged and provided critical context for interpreting spectral index trends and classification outcomes.

Spectral Data

Spectral information was extracted from both hyperspectral and multispectral imagery using LiDAR-derived canopy polygons, allowing for the calculation of a broad suite of spectral indices known to reflect stress-related physiological changes. More than 65 indices spanning multiple functional categories were computed, including those sensitive to pigment content (e.g., chlorophyll), leaf and canopy structure, xanthophyll-cycle activity, disease expression, and reflectance in the visible (RGB) spectrum (Table A1). Each canopy polygon corresponded to a single tree, with all spectral calculations and comparisons carried out at the individual tree level.

To evaluate treatment effects, Welch's t-tests (assuming unequal variance) were performed at each timepoint comparing *crop* and *cull* trees across all spectral bands and indices using R (version 4.3.3) (R Core Team, 2024). The resulting *p-values* were used to identify wavelengths and indices exhibiting statistically significant differences between treated and untreated trees over time. These differences were subsequently visualised through boxplots and spectral response curves.

Classification of *Cull* and *Crop* Trees

A linear Support Vector Machine (SVM) classifier was employed to differentiate *cull* trees from *crop* trees based on multispectral and hyperspectral imagery. Classification was performed at the individual tree level using features derived from each tree's canopy polygon, enabling us to capture variation between trees within each block. The linear SVM approach was selected for its effectiveness in high-dimensional settings where the number of features is comparable to, or exceeds, the number of samples (Vapnik, 1999). This method offers computational efficiency and a lower risk of overfitting relative to nonlinear kernels. The classifier seeks to determine an optimal hyperplane that maximizes the margin between the two classes.

Formally, given a training dataset (x_i, y_i) where x_i denotes the feature vector and y_i the corresponding class label, the SVM solves the following optimisation problem:

$$\min_{w,b} \frac{1}{2} \|w\|^2 + C \sum_{i=1}^n \xi_i \quad (1)$$

subject to the constraints:

$$y_i(w^T x_i + b) \geq 1 - \xi_i, \quad \xi_i \geq 0, \quad \text{for all } i$$

Here, w is the weight vector, b the bias term, ξ_i the slack variables allowing for misclassifications, and C a regularisation parameter balancing margin maximization with classification error.

Two datasets were used to generate predictor variables: multispectral and hyperspectral VNIR imagery. For the multispectral dataset, ten vegetation indices and the ten raw reflectance bands

were included, totalling 20 predictors. For the hyperspectral dataset, 67 Narrow Band Hyperspectral Indices (NBHIs) were computed and used as input variables. All predictors were standardised to ensure consistent feature scaling.

To address class imbalance between *crop* and *cull* trees, the majority class (*crop*) was randomly down sampled to match the number of *cull* trees. This resulted in balanced training datasets, though overall sample sizes per block were reduced, ranging from 50 to 66 trees.

Prior to model training, recursive feature elimination (RFE) was applied using a linear SVM to identify the most informative predictors. Feature importance was evaluated based on the absolute values of the weight vector $|w|$, and the least important variables were iteratively removed until no more than ten predictors remained. The final SVM model was trained using the reduced predictor set. Model performance was evaluated using a 5-fold cross-validation procedure, repeated 10 times to enhance robustness and reduce bias associated with any single train-test split. Accuracy metrics from the ten iterations were averaged to provide a reliable performance estimate.

Classification performance for *cull* trees was evaluated using Precision, Recall, and F1 Score, calculated as follows:

$$\text{Precision} = \frac{\text{TP}}{\text{TP} + \text{FP}} \quad (2)$$

$$\text{Recall} = \frac{\text{TP}}{\text{TP} + \text{FN}} \quad (3)$$

$$\text{F1 score} = 2 \times \frac{\text{Precision} \times \text{Recall}}{\text{Precision} + \text{Recall}} \quad (4)$$

where TP represents true positives, FP false positives, and FN false negatives.

Sensor Simulation: Exploring Cost-Effective Monitoring

To assess the potential of lower-cost, operationally accessible multispectral (MS) sensors for detecting herbicide-induced stress in radiata pine, a simulation exercise was undertaken. Hyperspectral imagery collected during the study was downsampled to replicate the spectral band configurations of several commercial MS sensors (e.g. MicaSense RedEdge, DJI Phantom 4 Multispectral, DJI Mavic 3M). Following the same approach as the primary (hyperspectral & multispectral) analysis, SVM classification models were then applied to evaluate the ability of each simulated sensor to distinguish chemically thinned (*cull*) trees from retained (*crop*) trees.

RESULTS

Ground Observations and Visual Assessments

Visual assessments conducted prior to herbicide application confirmed that both *crop* and *cull* trees were generally healthy, with minimal canopy discoloration (Figure 7a). Across the treatment blocks, an average of 93 percent of *crop* trees showed no discoloration, while only 7 percent displayed light symptoms. *Cull* trees exhibited slightly more variability, but on average 85 percent remained free of discoloration, with 15 percent showing light to moderate symptoms.

The first post-treatment assessment revealed a clear trend of increasing discoloration in the *cull* trees as the number of DAT progressed (Figure 7b). At 11 to 16 DAT (Blocks 5 and 6), most trees still exhibited no or light discoloration (less than 20 percent canopy area), although by 16 DAT, 29 percent of *cull* trees had already developed moderate symptoms. Beyond this point, the proportion of trees with more than 40 percent discoloration increased rapidly, 47 percent at 25 DAT, 71 percent at 30 DAT, 78 percent at 39 DAT, and 100 percent at 45 DAT, indicating a steady and intensifying physiological response to the herbicide.

In contrast, *crop* trees within the treated plots showed no meaningful change in condition. Across the six treated blocks, an average of 89 percent of *crop* trees displayed no discoloration in the first post-treatment assessment, and 11 percent showed only a light dull(er) green discoloration. The control block exhibited similar stability, with minimal changes between the pre- and post-treatment assessments.

The second post-treatment assessment confirmed the continuing progression of stress symptoms in *cull* trees, with all treated individuals exhibiting at least high levels of canopy discoloration (40–60 percent) between 53 and 87 DAT (Figure 7c). By this stage, the herbicide had clearly taken full effect, and all treated *cull* trees had transitioned into advanced stages of stress. In comparison, the condition of *crop* trees remained largely unchanged, with 88 percent showing no discoloration and only 12 percent displaying a light dull(er) green discoloration. Trees in the control block remained stable throughout.

Overall, the sequence of visual assessments confirmed that the chemical thinning treatment was highly effective in selectively inducing stress in the targeted *cull* trees, with canopy-level discoloration becoming increasingly pronounced beyond 16 DAT.

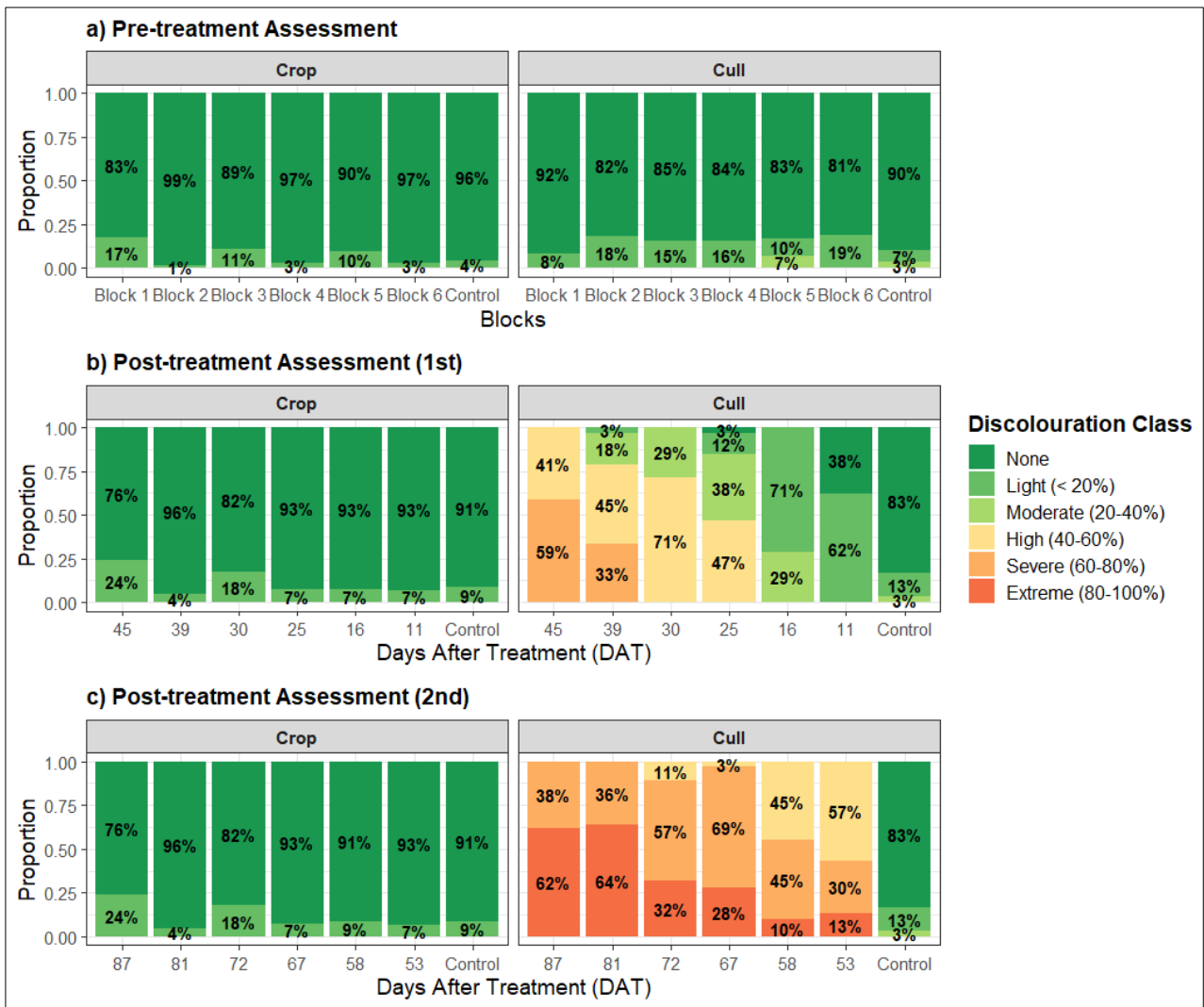


Figure 7. Proportions of canopy discolouration classes for *crop* and *cull* trees across all the treatment blocks, based on three visual assessments. Due to the staggered treatment schedule, the pre-treatment (a) is presented relative to the corresponding treatment blocks, while subsequent post-treatment assessments (b and c) are grouped by their respective days after treatment (DAT).

Treatment Differences in Multispectral Data

Analysis of the UAV-acquired multispectral data revealed progressive spectral differences between treated (*cull*) and untreated (*crop*) trees, which closely mirrored the visual discolouration patterns described earlier. In the early stages following herbicide application (13 and 18 days after treatment), no significant spectral differences were observed between *crop* and *cull* trees, and the reflectance curves for all groups remained similar to those in the untreated control block (Figure 8).

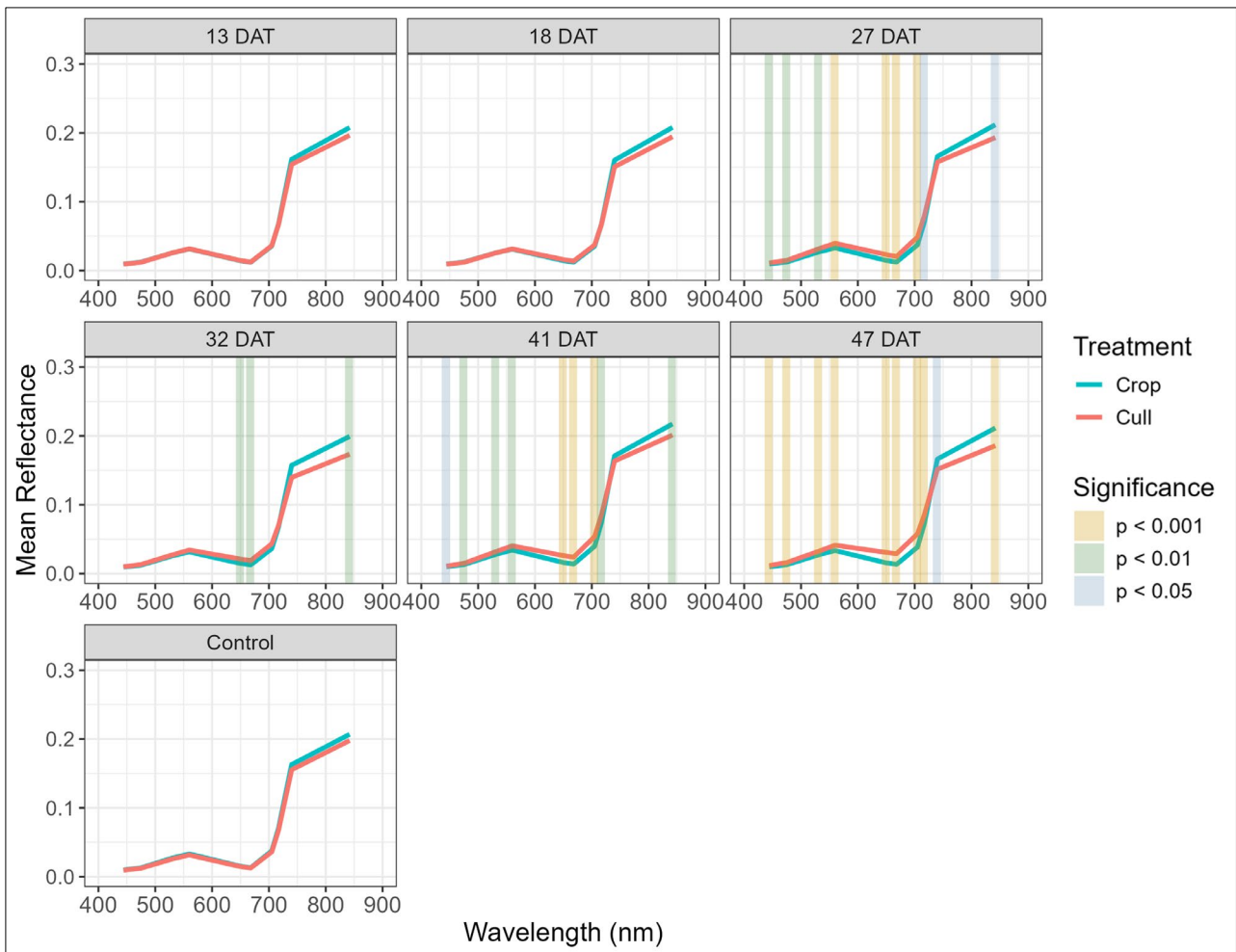


Figure 8. Variation in reflectance against wavelength, by treatment, for the untreated control and post-treatment blocks (13-47 days after treatment, DAT) at the time of the multispectral imagery capture. Vertical color-coded strips indicate wavelengths where significant differences between *crop* and *cull* trees were detected, with the strength of significance represented by colour: gold for $p < 0.001$, green for $p < 0.01$, and blue for $p < 0.05$.

From 27 DAT onwards, spectral differences became increasingly pronounced. Significant separation emerged in key wavelength regions, particularly within the visible red (e.g. 650 nm and 668 nm), red-edge (705 nm, 717 nm), and near-infrared (842 nm) bands. This pattern of divergence continued to strengthen through 41 and 47 DAT, at which point highly significant differences between *crop* and *cull* trees were observed across most multispectral bands (Figure 8).

Multispectral vegetation indices showed a similar trend (Figure 9; Table A2). In the early DAT periods, only the Photochemical Reflectance Index (PRI) and NDVI2 exhibited significant sensitivity to treatment effects, with PRI showing early divergence from 13 DAT ($p < 0.05$). By 27 DAT, a wider range of indices, including NDVI, GNDVI, NDWI, NDRE, and GNDVI2, showed high levels of statistical significance ($p < 0.01$) in distinguishing treated trees from *crop* trees. By the later timepoints (41 and 47 DAT), all multispectral indices demonstrated strong and consistent separation between the two groups (Figure 9).

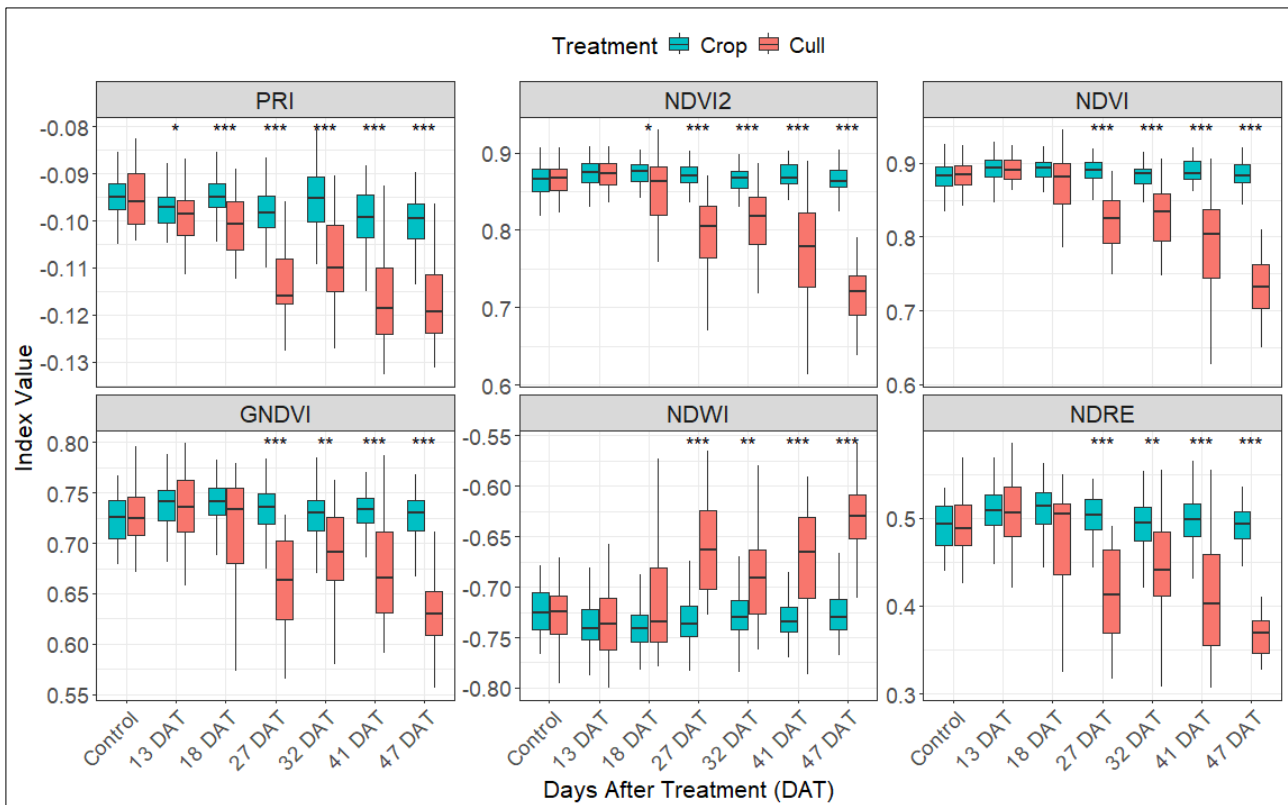


Figure 9. Variation in selected multispectral indices for *crop* and *cull* trees against the control block and each post-treatment period (13-47 days after treatment, DAT). Asterisks above each time point indicate the level of statistical significance between *crop* and *cull* treatments (* $p < 0.05$, ** $p < 0.01$, *** $p < 0.001$). Indices are ordered from top left to bottom right by increasing mean p -value across the DAT intervals.

Importantly, no significant spectral differences were found between treatments in the control block, confirming the stability of untreated trees and reinforcing the treatment-specific response observed in the *cull* trees.

Treatment Differences in Hyperspectral Data

The hyperspectral data showed trends that were consistent with the multispectral results, with limited separation between treated and untreated trees in the early stages, followed by progressively stronger treatment-related differences from 27 DAT onwards (Figure 10). From this point, significant divergence in spectral reflectance was observed between *cull* and *crop* trees across key wavelengths. Specifically, treated trees exhibited higher reflectance in the red region, lower reflectance in the near-infrared (NIR), and altered red-edge slope characteristics. These spectral changes are consistent with known physiological responses to herbicide, including reduced chlorophyll content, impaired photosynthesis, and needle degradation. In contrast, *crop* trees maintained stable reflectance profiles, suggesting continued canopy health and function.

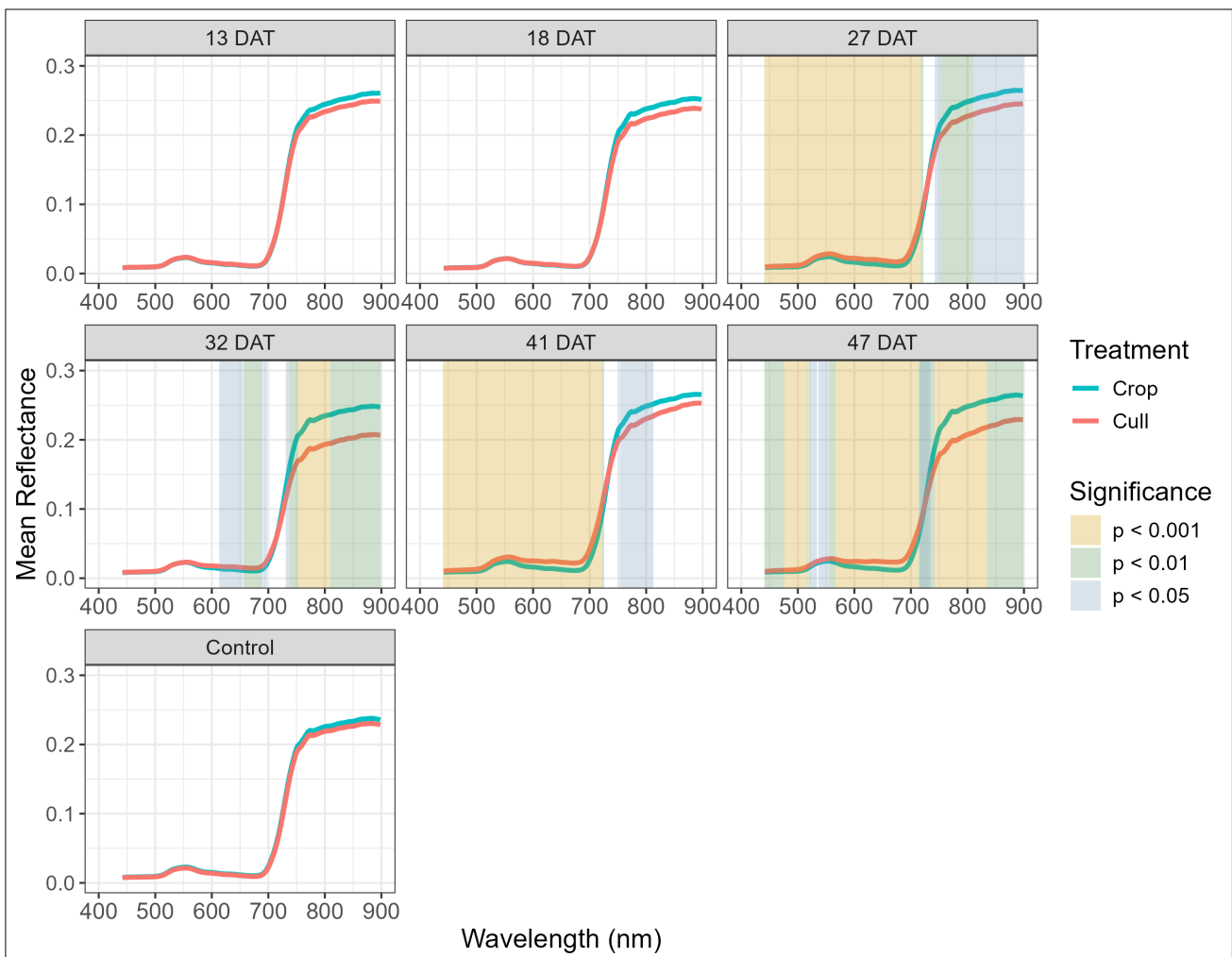


Figure 10. Variation in reflectance against wavelength, by treatment, for the untreated control and post-treatment blocks (13–47 days after treatment, DAT) at the time of the hyperspectral imagery capture. Vertical color-coded regions indicate wavelengths where significant differences between *crop* and *cull* trees were detected, with the strength of significance represented by colour: gold for $p < 0.001$, green for $p < 0.01$, and blue for $p < 0.05$.

Analysis of hyperspectral vegetation indices also revealed early and progressive treatment effects (Figure 11, Table A3). At 13 DAT, nine indices already showed significant differences between *crop* and *cull* trees. Most of these were pigment-sensitive indices, including four variants of the Photochemical Reflectance Index (PRI), such as PRICI, PRIn, PRI570, and SR528_574. By 18 DAT, eleven indices were significant, five of which had also been significant at 13 DAT, but with stronger statistical separation.

From 27 DAT onwards, the majority of hyperspectral indices showed highly significant differences between treatments ($p < 0.001$) (Figure 11, Table A3). When indices were ranked by average p-value across the full post-treatment period (13–47 DAT), PRI-related indices consistently appeared among the top performers. Of the ten highest-ranking indices, seven were pigment-based, two were RGB-derived (BRI and LIC5), and one was linked to disease-related canopy stress (HI). These results underscore the role of pigment degradation and canopy discolouration as key indicators of herbicide-induced stress.

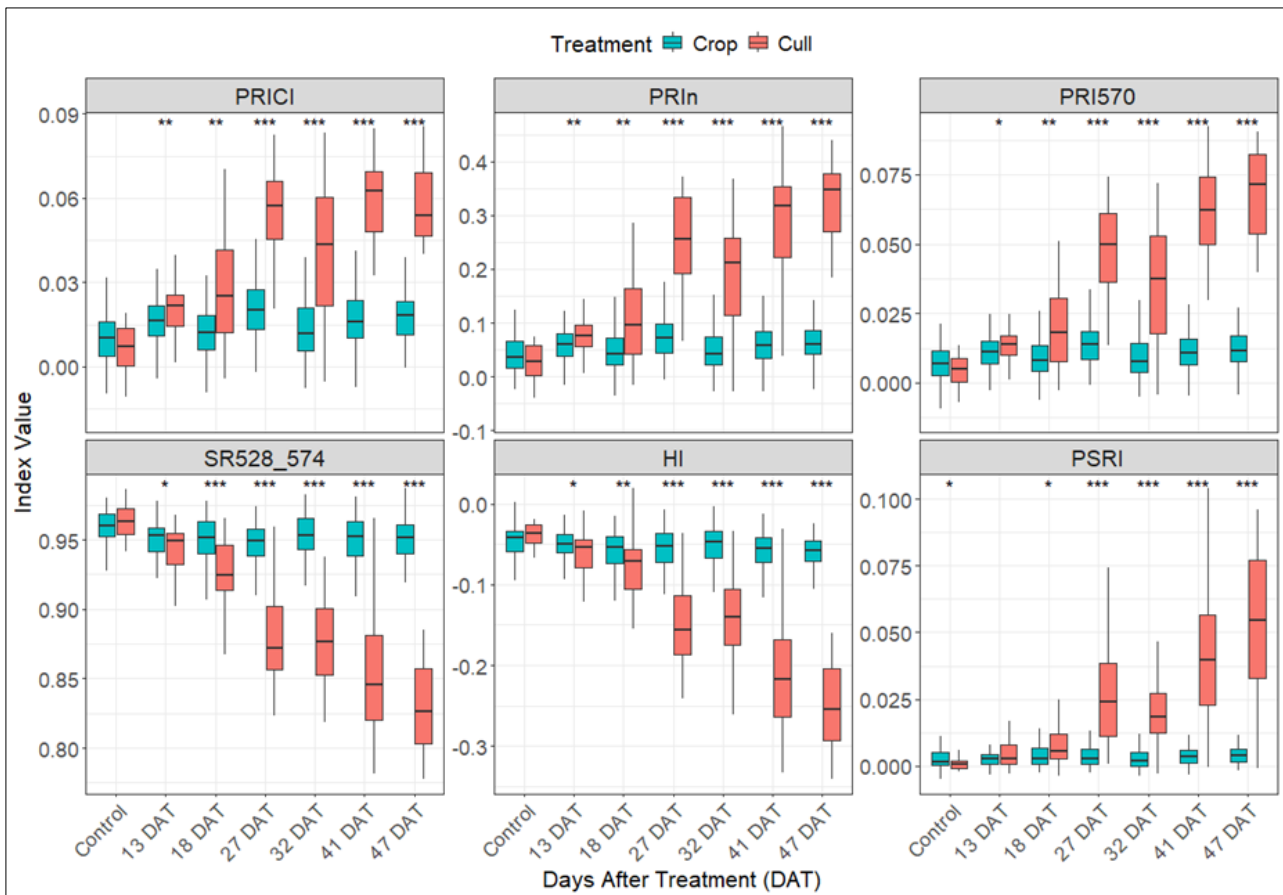


Figure 11. Variation in selected hyperspectral indices for *crop* and *cull* trees against the control block and each post-treatment period (13-47 days after treatment, DAT). Asterisks above each time point indicate the level of statistical significance between *crop* and *cull* treatments ($*p < 0.05$, $**p < 0.01$, $***p < 0.001$). The indices are ordered from top left to bottom right by increasing mean p -value across the DAT intervals.

Overall, the hyperspectral data supported a clear progression of physiological stress responses in treated trees, with strong discriminatory power from both wavelength-level and index-based analyses. These results reinforce the potential for UAV-based hyperspectral imaging to detect early stress prior to visible canopy changes and provide a broader suite of spectral indicators for monitoring treatment effectiveness.

Classification of *Cull* from *Crop* Trees

Classification Results using Multispectral Data

Classification models based on multispectral imagery were able to identify treated (*cull*) trees with good accuracy from 18 DAT (Table 2). At this time point, the model achieved an F1 score greater than 0.70, indicating reliable early detection. Model performance improved progressively, reaching its highest accuracy at 47 DAT, with a perfect precision score of 1.00 and an F1 score of 0.94. Across all time points, precision consistently exceeded recall, meaning the models were cautious in identifying treated trees. While few false positives were produced, some true *cull* trees were missed.

The Photochemical Reflectance Index (PRI) was consistently ranked among the top predictor variables and was the most influential predictor at 18, 27, and 32 DAT (Table 2). This highlights its value as a sensitive indicator of early stress based on multispectral data.

Table 2. Confusion matrix and classification results from the SVM model for distinguishing crop and cull trees using multispectral (Multi.) and hyperspectral (Hyp.) data across post-treatment periods (13–47 days after treatment, DAT). Abbreviations include: true positive (TP), false positive (FP), false negative (FN), and true negative (TN). Reported classification metrics are precision (Prec.), recall (Rec.), and F1 score. Shading indicates model performance—blue for good ($0.7 < F1 \leq 0.8$), green for excellent ($0.8 < F1 \leq 0.9$), and gold for outstanding ($F1 \geq 0.9$). The top three contributing variables are listed for each timepoint, with their normalised importance scores (Norm. Score) in brackets.

Sensor	DAT	Confusion Matrix (%)				Classification Statistics			Important Variables (Norm. Score)
		TN	FP	FN	TP	Prec.	Rec.	F1	
Multi.	13	36.8	13.2	23.0	27.0	0.67	0.54	0.60	R842 (1.0), R705 (0.84), PRI (0.21)
	18	42.9	7.1	13.4	36.6	0.84	0.73	0.78	PRI (1.0), GRVI (0.78), R650 (0.73)
	27	47.4	2.6	8.1	41.9	0.94	0.84	0.89	PRI (1.0), NDRE (0.67), R444 (0.61)
	32	41.8	8.2	4.4	45.6	0.85	0.91	0.88	PRI (1.0), R842 (0.89), RE (0.60)
	41	46.8	3.2	10.9	39.1	0.92	0.78	0.85	GNDVI (1.0), FMCI (0.40), PRI (0.29)
	47	50.0	0.0	5.4	44.6	1.00	0.89	0.94	NDVI2 (1.0), PRI (0.25), FMCI (0.1)
Hyp.	13	38.5	11.5	14.3	35.7	0.76	0.71	0.73	R (1.0), OSAVI (0.67), SR510_574 (0.5)
	18	41.3	8.7	12.1	37.9	0.81	0.76	0.78	PSSRc (1.0), HI (0.89), CRI700_515 (0.75)
	27	47.9	2.1	10.3	39.7	0.95	0.79	0.86	PRI570 (1.0), B (0.42), PSRI (0.38)
	32	48.8	1.2	2.6	47.4	0.98	0.95	0.96	SR528_574 (1.0), PRICI (0.83), TCARI (0.82)
	41	48.5	1.5	4.7	45.3	0.97	0.91	0.94	PRICI (1.0), DCab (0.89), LIC6 (0.78)
	47	49.8	0.2	3.6	46.4	1.00	0.93	0.96	PRIm2 (1.0), DCab (0.31), SR510_574 (0.31)

Classification Results using Hyperspectral Data

Predictions based on hyperspectral narrowband indices (NBHIs) generally outperformed those using multispectral reflectance and vegetation indices (Table 2). Cull trees were accurately detected as early as 13 days after treatment (DAT)—five days earlier than with multispectral data. Accuracy improved over time, peaking at 47 DAT with a precision of 1.00 and F1 score of 0.96. As with multispectral data, precision consistently exceeded recall throughout the assessment period.

Early classification (13–18 DAT) was driven by indices sensitive to pigment and structural changes, such as R, OSAVI, SR510_574, PSSRc, and CRI700_515 (Table 2). By 27 DAT, accuracy improved with the inclusion of PRI570, the Blue Index (B), and PSRI, indicating ongoing pigment degradation. From 32 DAT onward, classification was dominated by narrowband indices linked to pigment and structure (e.g., SR528_574, PRICI, and TCARI). By 47 DAT, these were joined by DCab, LIC6, and the re-emergent SR510_574, capturing the combined effects of pigment loss, moisture reduction, and canopy decline. This progression in important variables likely reflects the physiological development of herbicide stress over time (Table 2).

These results demonstrate the effectiveness of UAV-based spectral classification for identifying herbicide-treated trees, with hyperspectral data offering earlier and slightly more accurate detection than multispectral imagery.

Sensor Simulation Results

The performance of the simulated lower-cost multispectral sensors is presented in Table 3. It should be noted that the multispectral analysis in the study described above was based on a 10-band sensor, whereas the simulated configurations were restricted to 4 or 5 bands, reflecting the limited spectral resolutions of more accessible systems. Despite this reduction in spectral resolution, two of the three simulated sensors achieved similarly strong performance as early as 18 DAT, and by 27 DAT all three configurations produced F1 scores above 0.80. At 47 DAT, all simulated sensors reached an F1 score of 0.92, closely matching the 10-band multispectral result ($F1 = 0.94$) and approaching the hyperspectral system's performance ($F1 = 0.96$) (Table 3).

Table 3: Simulated classification results using downsampled hyperspectral data to represent lower-cost multispectral sensors across post-treatment periods (13–47 days after treatment, DAT). Blue shading indicates

good performance ($0.7 < F1 \leq 0.8$), green indicates excellent performance ($0.8 < F1 \leq 0.9$), and gold indicates outstanding performance ($F1 \geq 0.9$).

Simulated Sensor	DAT	Precision	Recall	F1
<i>MicaSense Altum / RE</i>				
	13 DAT	0.72	0.6	0.65
	18 DAT	0.65	0.65	0.65
	27 DAT	0.92	0.7	0.8
	32 DAT	0.87	0.91	0.89
	41 DAT	0.96	0.82	0.88
	47 DAT	0.96	0.89	0.92
<i>DJI P4 (Multispectral)</i>				
	13 DAT	0.71	0.55	0.62
	18 DAT	0.72	0.69	0.71
	27 DAT	0.91	0.71	0.79
	32 DAT	0.9	0.89	0.89
	41 DAT	0.94	0.85	0.89
	47 DAT	0.96	0.88	0.92
<i>DJI Mavic3M</i>				
	13 DAT	0.63	0.56	0.59
	18 DAT	0.7	0.71	0.71
	27 DAT	0.91	0.71	0.8
	32 DAT	0.87	0.93	0.9
	41 DAT	0.94	0.85	0.89
	47 DAT	0.95	0.9	0.92

DISCUSSION AND CONCLUSIONS

This study demonstrated that UAV-based multispectral and hyperspectral imagery can be used effectively to detect herbicide-induced stress in nine-year-old radiata pine at early stages. While most prior work on herbicide stress has focused on agricultural *crops*, research in forestry contexts remains limited. Previous studies have either simulated herbicide stress using multispectral imagery in field settings (Dash et al., 2017) or used hyperspectral data in controlled trials on potted trees (Scholten et al., 2019). To our knowledge, this is among the first studies to apply both sensor types in an operational forest to distinguish treated (*cull*) from retained (*crop*) trees during early physiological decline.

Changes in reflectance, vegetation indices, and model predictions closely aligned with the progression of visible canopy symptoms. Strong classification accuracy and highly significant differences between crop and cull trees were observed once moderate to severe discolouration appeared. Earlier stages of stress showed slightly lower, but still meaningful, separability, especially when using pigment- and structure-sensitive indices. Hyperspectral data, with its higher spectral resolution, was particularly effective in detecting these early signs of stress as early as 13 days after treatment. This reinforces previous findings that hyperspectral imagery is generally better suited than multispectral systems for detecting early physiological stress (Honkavaara et al., 2020; Poblete et al., 2020; Duarte et al., 2022; W. Wu et al., 2020).

Multispectral classification performance exceeded an F1 score of 0.70 from 18 days after treatment (DAT) onward, improving through to 47 DAT. Early detection relied on both vegetation indices and individual bands. Notably, near-infrared reflectance (R842), linked to canopy structure (Slaton et al., 2001), and red-edge bands (R705, R650), associated with chlorophyll content (Datt, 1998; Gitelson et al., 2003), were among the top predictors at 13–18 DAT. This shows that even broad-band multispectral sensors can detect early stress signals when red-edge and NIR wavelengths are included. At later stages, variable importance shifted toward greenness and structure indices such as GNDVI and NDVI2, aligning with visible canopy decline.

Hyperspectral imagery enabled earlier and more consistent stress detection, reaching an F1 of 0.96 from 32 DAT. Early classification was driven by pigment-sensitive indices (e.g., PSSRc,

CRI700_515) and narrowband PRI variants (e.g., SR510_574), while later stages were marked by indices linked to pigment loss, moisture decline, and structural breakdown (e.g., PRICI, DCab, LIC6). This shift reflects the known physiological progression of herbicide stress, from early photosynthetic disruption to visible canopy damage, as also observed in previous hyperspectral studies (Scholten et al., 2019).

PRI-related indices, which respond to changes in xanthophyll cycle activity, light-use efficiency, and carotenoid pigments (Gamon et al., 1992; Garbulsky et al., 2011), consistently ranked among the top performers across both hyperspectral and multispectral data. Their strong performance likely reflects early physiological disruption caused by metsulfuron-methyl. This sulfonylurea herbicide inhibits acetolactate synthase (ALS), blocking protein synthesis and cell division, and ultimately impairing photosynthetic function (Russell et al., 2002; Sherwani et al., 2015; Traxler et al., 2023). These disruptions, such as reduced CO₂ fixation, electron transport efficiency, and chlorophyll content, have been previously linked to detectable changes in PRI (Riethmuller-Haage et al., 2006).

While hyperspectral sensors provide higher sensitivity, the strong performance of the multispectral dataset highlights its value as a cost-effective and practical tool for forest health monitoring. This is supported by recent UAV studies, such as those by Yu et al. (2024), Arapostathi et al. (2024), and Bozzini et al. (2025), which demonstrated early detection of stress and pest damage using red-edge and pigment-sensitive indices from multispectral imagery. At larger scales, Bhattarai et al. (2020) also found red-edge indices from Sentinel-2 effective for mapping spruce budworm defoliation, reinforcing the relevance of these indices across both UAV and satellite platforms.

Simulations based on downsampled hyperspectral data were used to reproduce three commercially available multispectral (MS) sensors with 4–5 bands. Namely the MicaSense Altum/RedEdge, DJI Phantom 4 Multispectral, and DJI Mavic 3M, which are all priced in the \$10–15k range. These were compared against the 10-band MS system (~\$50k) described above in the main study and a full hyperspectral system (~\$600k). Despite having fewer bands, the simulated sensors performed strongly, particularly from 27 DAT onwards. By 47 DAT, all three achieved F1 scores of 0.92, closely matching the 10-band MS system (F1 = 0.94) and approaching the hyperspectral benchmark (F1 = 0.96). These results highlight that, while finer spectral resolution offers advantages in early detection and trait derivation, well-timed monitoring using strategically selected bands can still yield high-confidence classification of chemically thinned (*cull*) versus retained (*crop*) trees. The findings suggest that low-cost sensors could offer a practical and affordable way to scale up remote sensing for monitoring chemical thinning, particularly in situations where high-end systems are not available.

Thermal sensors, which detect canopy temperature increases associated with stomatal closure and reduced transpiration (Hernández-Clemente et al., 2019; Smigaj et al., 2019; Still et al., 2019), may also offer complementary insights. Given the known overlap between thermal responses and PRI-detectable pigment changes (Gamon et al., 1992; Maes & Steppe, 2012; Nakamura et al., 2024), future efforts to integrate thermal and spectral data could further enhance early stress detection, particularly as compact and affordable thermal sensors continue to improve (Smigaj et al., 2023). In this study, thermal imagery was collected, although challenges with data quality limited its utility. As with hyperspectral systems, extracting subtle physiological signals from thermal data requires careful planning around calibration targets and procedures, which are still being refined at operational scales.

These results are relevant to the growing interest in chemical thinning as a forest management strategy in New Zealand (Holt & Dickinson, 2024). Early detection of herbicide-induced stress could improve operational efficiency by reducing the need for follow-up inspections and avoiding overtreatment, especially in remote or difficult terrain. The lack of discolouration in control plots and untreated *crop* trees suggests limited off-target effects, though further monitoring is needed to assess longer-term effects. It should be noted that the strength of spectral separation between *crop* and *cull* trees may vary with local site conditions, such as soil type, seasonal timing, terrain, and background health of the stand. Stronger classification results are more likely when stress is limited to a subset of trees within an otherwise healthy canopy, as this creates clearer contrast. In more degraded stands, however, physiological differences between *crop* and *cull* trees may be less

distinct, making it harder to achieve good class separation using UAV-based multispectral or hyperspectral imagery.

This study establishes a basis for applying UAV-based spectral imaging to support chemical thinning in operational forestry. The identified early detection window of 13 to 18 days after treatment offers a practical reference point for monitoring effectiveness and provides a foundation for future research, including potential applications in detecting other forms of tree stress such as pests and diseases. While hyperspectral imagery provides valuable insights into early stress responses and trait derivation, its widespread operational use remains constrained by high costs, data volume, and processing complexity. For this reason, the study incorporated both a 10-band multispectral sensor and a simulation exercise, using downsampled hyperspectral data, to evaluate the performance of lower-cost commercial multispectral systems. The findings highlight the potential for integrating these cost-effective tools into routine forest health monitoring, while also demonstrating the added value of hyperspectral data for refining early detection methods. Future work should explore how these results generalise across different environmental conditions, particularly in more topographically complex sites where UAV-based monitoring may offer the greatest benefits.

ACKNOWLEDGEMENTS

This project was funded through the Ministry of Business, Innovation and Employment (MBIE) programme, grant number C04X2101 (Seeing the forest for the trees: transforming tree phenotyping for future forests). Valuable co-funding from the Precision Silviculture Programme within Forest Growers Research (CN 013574), as well as in-kind support from Rayonier Matariki Forests made the project a reality and logistically possible.

We greatly appreciate inputs from Toby Stovold in the design of the experiment. Rayonier Matariki Forests, Rob Schoonderwoerd and Acacia Farmery provided invaluable assistance in terms of field planning and safe site access. We thank Travis Brake (Advanced Technicians Ltd) for conducting the visual assessments. We also thank Peter Massam, Warren Yorston, Kevin Park, Honey-Jane Estarija, Richard Vili for their efforts in establishing the experimental blocks and plots, and for collecting the UAV data. Sadeepa Jayathunga is also sincerely acknowledged for her assistance with LiDAR data processing and the generation of canopy polygons. Thanks also to Nicolò Camarretta for his reviews and useful feedback.

REFERENCES

- Adão, T., Hruška, J., Pádua, L., Bessa, J., Peres, E., Morais, R., & Sousa, J. J. (2017). Hyperspectral Imaging: A Review on UAV-Based Sensors, Data Processing and Applications for Agriculture and Forestry. *Remote Sensing*, 9(11), Article 11. <https://doi.org/10.3390/rs9111110>
- Arapostathi, E., Panopoulou, C., Antonopoulos, A., Katsileros, A., Karellas, K., Dimopoulos, C., & Tsagkarakis, A. (2024). Early Detection of Potential Infestation by *Capnodis tenebrionis* (L.) (Coleoptera: Buprestidae), in Stone and Pome Fruit Orchards, Using Multispectral Data from a UAV. *Agronomy*, 14(1), Article 1. <https://doi.org/10.3390/agronomy14010020>
- Behmann, J., Steinrücken, J., & Plümer, L. (2014). Detection of early plant stress responses in hyperspectral images. *ISPRS Journal of Photogrammetry and Remote Sensing*, 93, 98–111. <https://doi.org/10.1016/j.isprsjprs.2014.03.016>
- Beveridge, A. E., & Hedderwick, G. W. (1962, July 24). Chemical methods of vegetation control in New Zealand forestry (Personal Communication). *Discussion on Chemical Methods of Vegetation Control*.
- Bhattarai, R., Rahimzadeh-Bajgiran, P., Weiskittel, A., & MacLean, D. A. (2020). Sentinel-2 based prediction of spruce budworm defoliation using red-edge spectral vegetation indices. *Remote Sensing Letters*, 11(8), 777–786. <https://doi.org/10.1080/2150704X.2020.1767824>
- Blackburn, G. A. (1998). Spectral indices for estimating photosynthetic pigment concentrations: A test using senescent tree leaves. *International Journal of Remote Sensing*, 19(4), 657–675. <https://doi.org/10.1080/014311698215919>
- Blackburn, G. A. (1999). Relationships between Spectral Reflectance and Pigment Concentrations in Stacks of Deciduous Broadleaves. *Remote Sensing of Environment*, 70(2), 224–237. [https://doi.org/10.1016/S0034-4257\(99\)00048-6](https://doi.org/10.1016/S0034-4257(99)00048-6)
- Blackburn, G. A. (2007). Hyperspectral remote sensing of plant pigments. *Journal of Experimental Botany*, 58(4), 855–867. <https://doi.org/10.1093/jxb/erl123>
- Bozzini, A., Huo, L., Brugnaro, S., Morgante, G., Persson, H. J., Finozzi, V., Battisti, A., & Faccoli, M. (2025). Multispectral drone images for the early detection of bark beetle infestations:

Assessment over large forest areas in the South-Eastern Alps. *Frontiers in Forests and Global Change*, 8(1532954). <https://doi.org/10.3389/ffgc.2025.1532954>

Broge, N. H., & Leblanc, E. (2001). Comparing prediction power and stability of broadband and hyperspectral vegetation indices for estimation of green leaf area index and canopy chlorophyll density. *Remote Sensing of Environment*, 76(2), 156–172.

[https://doi.org/10.1016/S0034-4257\(00\)00197-8](https://doi.org/10.1016/S0034-4257(00)00197-8)

Buddenbaum, H., Stern, O., Paschmionka, B., Hass, E., Gattung, T., Stoffels, J., Hill, J., & Werner, W. (2015). Using VNIR and SWIR field imaging spectroscopy for drought stress monitoring of beech seedlings. *International Journal of Remote Sensing*, 36(18), 4590–4605.

<https://doi.org/10.1080/01431161.2015.1084435>

Calderón, R., Navas-Cortés, J. A., Lucena, C., & Zarco-Tejada, P. J. (2013). High-resolution airborne hyperspectral and thermal imagery for early detection of Verticillium wilt of olive using fluorescence, temperature and narrow-band spectral indices. *Remote Sensing of Environment*, 139, 231–245. <https://doi.org/10.1016/j.rse.2013.07.031>

Carter, G. A., Cibula, W. G., & Dell, T. R. (1996). Spectral reflectance characteristics and digital imagery of a pine needle blight in the southeastern United States. *Canadian Journal of Forest Research*, 26(3), 402–407. <https://doi.org/10.1139/x26-045>

Carter, G. A., & Miller, R. L. (1994). Early detection of plant stress by digital imaging within narrow stress-sensitive wavebands. *Remote Sensing of Environment*, 50(3), 295–302.

[https://doi.org/10.1016/0034-4257\(94\)90079-5](https://doi.org/10.1016/0034-4257(94)90079-5)

Chappelle, E. W., Kim, M. S., & McMurtrey, J. E. (1992). Ratio analysis of reflectance spectra (RARS): An algorithm for the remote estimation of the concentrations of chlorophyll A, chlorophyll B, and carotenoids in soybean leaves. *Remote Sensing of Environment*, 39(3), 239–247. [https://doi.org/10.1016/0034-4257\(92\)90089-3](https://doi.org/10.1016/0034-4257(92)90089-3)

Chen, J. M. (1996). Evaluation of vegetation indices and a modified simple ratio for boreal applications. *Canadian Journal of Remote Sensing*, 22(3), 229–242.

<https://doi.org/10.1080/07038992.1996.10855178>

Coops, N., Stanford, M., Old, K., Dudzinski, M., Culvenor, D., & Stone, C. (2003). Assessment of Dothistroma Needle Blight of *Pinus radiata* Using Airborne Hyperspectral Imagery.

Phytopathology, 93(12), 1524–1532. Scopus.

<https://doi.org/10.1094/PHYTO.2003.93.12.1524>

da Silva, S. D. P., de Paula Amaral, L., Aparecida Fantinel, R., & Coelho Eugenio, F. (2024).

RPAS-Based forest plantation health monitoring: An overview of recent progress.

International Journal of Remote Sensing, 45(24), 9131–9161.

<https://doi.org/10.1080/01431161.2024.2406036>

Dash, J. P., Watt, M. S., Pearse, G. D., Heaphy, M., & Dungey, H. S. (2017). Assessing very high resolution UAV imagery for monitoring forest health during a simulated disease outbreak.

ISPRS Journal of Photogrammetry and Remote Sensing, 131, 1–14.

<https://doi.org/10.1016/j.isprsjprs.2017.07.007>

Datt, B. (1998). Remote sensing of chlorophyll a, chlorophyll b, chlorophyll a+b, and total carotenoid content in eucalyptus leaves. *Remote Sensing of Environment*, 66(2), 111–121.

[https://doi.org/10.1016/S0034-4257\(98\)00046-7](https://doi.org/10.1016/S0034-4257(98)00046-7)

Daughtry, C. S. T., Walthall, C. L., Kim, M. S., de Colstoun, E. B., & McMurtrey, J. E. (2000).

Estimating corn leaf chlorophyll concentration from leaf and canopy reflectance. *Remote Sensing of Environment*, 74(2), 229–239. [https://doi.org/10.1016/S0034-4257\(00\)00113-9](https://doi.org/10.1016/S0034-4257(00)00113-9)

Duarte, A., Borralho, N., Cabral, P., & Caetano, M. (2022). Recent Advances in Forest Insect Pests and Diseases Monitoring Using UAV-Based Data: A Systematic Review. *Forests*, 13(6),

Article 6. <https://doi.org/10.3390/f13060911>

Ecke, S., Dempewolf, J., Frey, J., Schwaller, A., Endres, E., Klemmt, H.-J., Tiede, D., & Seifert, T.

(2022). UAV-Based Forest Health Monitoring: A Systematic Review. *Remote Sensing*, 14(13), 3205. <https://doi.org/10.3390/rs14133205>

Felix, M. J. B., Main, R., Watt, M. S., Arpanaei, M.-M., & Patuawa, T. (2025). Early Detection of Water Stress in Kauri Seedlings Using Multitemporal Hyperspectral Indices and Inverted

Plant Traits. *Remote Sensing*, 17(3), Article 3. <https://doi.org/10.3390/rs17030463>

Filella, I., & Peñuelas, J. (1994). The red edge position and shape as indicators of plant chlorophyll content, biomass, and hydric status. *International Journal of Remote Sensing*, 15(7), 1459–

1470. <https://doi.org/10.1080/01431169408954177>

- Gamon, J. A., Peñuelas, J., & Field, C. B. (1992). A narrow-waveband spectral index that tracks diurnal changes in photosynthetic efficiency. *Remote Sensing of Environment*, 41(1), 35–44. [https://doi.org/10.1016/0034-4257\(92\)90059-S](https://doi.org/10.1016/0034-4257(92)90059-S)
- Gamon, J. A., Serrano, L., & Surfus, J. S. (1997). The Photochemical Reflectance Index: An Optical Indicator of Photosynthetic Radiation Use Efficiency across Species, Functional Types, and Nutrient Levels. *Oecologia*, 112(4), 492–501. <https://doi.org/10.1007/s004420050337>
- Garbulsky, M. F., Peñuelas, J., Gamon, J., Inoue, Y., & Filella, I. (2011). The photochemical reflectance index (PRI) and the remote sensing of leaf, canopy and ecosystem radiation use efficiencies: A review and meta-analysis. *Remote Sensing of Environment*, 115(2), 281–297. <https://doi.org/10.1016/j.rse.2010.08.023>
- Garrity, S. R., Eitel, J. U. H., & Vierling, L. A. (2011). Disentangling the relationships between plant pigments and the photochemical reflectance index reveals a new approach for remote estimation of carotenoid content. *Remote Sensing of Environment*, 115(2), 628–635. <https://doi.org/10.1016/j.rse.2010.10.007>
- Gitelson, A. A., Gritz, Y., & Merzlyak, M. N. (2003). Relationships between leaf chlorophyll content and spectral reflectance and algorithms for non-destructive chlorophyll assessment in higher plant leaves. *Journal of Plant Physiology*, 160(3), 271–282. <https://doi.org/10.1078/0176-1617-00887>
- Gitelson, A. A., Keydan, G. P., & Merzlyak, M. N. (2006). Three-band model for noninvasive estimation of chlorophyll, carotenoids, and anthocyanin contents in higher plant leaves. *Geophysical Research Letters*, 33(11), L11402. <https://doi.org/10.1029/2006GL026457>
- Gitelson, A. A., & Merzlyak, M. N. (1997). Remote estimation of chlorophyll content in higher plant leaves. *International Journal of Remote Sensing*, 18(12), 2691–2697. <https://doi.org/10.1080/014311697217558>
- Gitelson, A. A., Yacobi, Y. Z., Schalles, J. F., Rundquist, D. C., Han, L., Stark, R., & Etzion, D. (2000). Remote estimation of phytoplankton density in productive waters. *Advances in Limnology*, 55, 121–136.

- Gitelson, A. A., Zur, Y., Chivkunova, O. B., & Merzlyak, M. N. (2002). Assessing Carotenoid Content in Plant Leaves with Reflectance Spectroscopy. *Photochemistry and Photobiology*, 75(3), 272–281. [https://doi.org/10.1562/0031-8655\(2002\)0750272ACCIPL2.0.CO2](https://doi.org/10.1562/0031-8655(2002)0750272ACCIPL2.0.CO2)
- Goetz, A. F. H., Vane, G., Solomon, J. E., & Rock, B. N. (1985). Imaging Spectrometry for Earth Remote Sensing. *Science*, 228(4704), 1147–1153. <https://doi.org/10.1126/science.228.4704.1147>
- Haboudane, D., Miller, J. R., Pattey, E., Zarco-Tejada, P. J., & Strachan, I. B. (2004). Hyperspectral vegetation indices and novel algorithms for predicting green LAI of crop canopies: Modeling and validation in the context of precision agriculture. *Remote Sensing of Environment*, 90(3), 337–352. <https://doi.org/10.1016/j.rse.2003.12.013>
- Haboudane, D., Miller, J. R., Tremblay, N., Zarco-Tejada, P. J., & Dextraze, L. (2002). Integrated narrow-band vegetation indices for prediction of crop chlorophyll content for application to precision agriculture. *Remote Sensing of Environment*, 81(2–3), 416–426. [https://doi.org/10.1016/S0034-4257\(02\)00018-4](https://doi.org/10.1016/S0034-4257(02)00018-4)
- Hernández-Clemente, R., Hornero, A., Mottus, M., Penuelas, J., González-Dugo, V., Jiménez, J. C., Suárez, L., Alonso, L., & Zarco-Tejada, P. J. (2019). Early Diagnosis of Vegetation Health From High-Resolution Hyperspectral and Thermal Imagery: Lessons Learned From Empirical Relationships and Radiative Transfer Modelling. *Current Forestry Reports*, 5(3), 169–183. <https://doi.org/10.1007/s40725-019-00096-1>
- Hernández-Clemente, R., Navarro-Cerrillo, R. M., Suárez, L., Morales, F., & Zarco-Tejada, P. J. (2011). Assessing structural effects on PRI for stress detection in conifer forests. *Remote Sensing of Environment*, 115(9), 2360–2375. <https://doi.org/10.1016/j.rse.2011.04.036>
- Holt, L., & Dickinson, Y. (2024). Current Practices and Challenges in NZ Thinning Operations: Results of a Survey and Workshop in 2023. *Forest Growers Research: Precision Silviculture Programme (PSP-T022)*.
- Honkavaara, E., Näsi, R., Oliveira, R., Viljanen, N., Suomalainen, J., Khoramshahi, E., Hakala, T., Nevalainen, O., Markelin, L., Vuorinen, M., Kankaanhuhta, V., Lyytikäinen-Saarenmaa, P., & Haataja, L. (2020). Using multitemporal hyper- and multispectral uav imaging for detecting bark beetle infestation on norway spruce. *The International Archives of the*

Photogrammetry, Remote Sensing and Spatial Information Sciences, XLIII-B3-2020, 429–434. XXIV ISPRS Congress, Commission III (Volume XLIII-B3-2020) - 2020 edition.
<https://doi.org/10.5194/isprs-archives-XLIII-B3-2020-429-2020>

- Jordan, C. F. (1969). Derivation of leaf-area index from quality of light on the forest floor. *Ecology*, 50(4), 663–666. <https://doi.org/10.2307/1936256>
- Kim, Y., Glenn, D. M., Park, J., Ngugi, H. K., & Lehman, B. L. (2011). Hyperspectral image analysis for water stress detection of apple trees. *Computers and Electronics in Agriculture*, 77(2), 155–160. <https://doi.org/10.1016/j.compag.2011.04.008>
- Lad, L. E., Tinkham, W. T., Sparks, A. M., & Smith, A. M. S. (2023). Evaluating Predictive Models of Tree Foliar Moisture Content for Application to Multispectral UAS Data: A Laboratory Study. *Remote Sensing*, 15(24), 5703. <https://doi.org/10.3390/rs15245703>
- Lassalle, G. (2021). Monitoring natural and anthropogenic plant stressors by hyperspectral remote sensing: Recommendations and guidelines based on a meta-review. *Science of The Total Environment*, 788, 147758. <https://doi.org/10.1016/j.scitotenv.2021.147758>
- Lausch, A., Erasmi, S., King, D. J., Magdon, P., & Heurich, M. (2016). Understanding Forest Health with Remote Sensing -Part I—A Review of Spectral Traits, Processes and Remote-Sensing Characteristics. *Remote Sensing*, 8(12), Article 12.
<https://doi.org/10.3390/rs8121029>
- Le, T. S., Harper, R., & Dell, B. (2023). Application of Remote Sensing in Detecting and Monitoring Water Stress in Forests. *Remote Sensing*, 15(13), Article 13.
<https://doi.org/10.3390/rs15133360>
- Lichtenthaler, H. K. (1996). Vegetation stress: An introduction to the stress concept in plants. *Journal of Plant Physiology*, 148(1–2), 4–14. [https://doi.org/10.1016/S0176-1617\(96\)80287-2](https://doi.org/10.1016/S0176-1617(96)80287-2)
- Liu, J., & Huete, A. R. (1995). A feedback based modification of the NDVI to minimize canopy background and atmospheric noise. *IEEE Transactions on Geoscience and Remote Sensing*, 33(2), 457–465. <https://doi.org/10.1109/TGRS.1995.8746027>
- Maclaren, P., Baker, G., Dean, M., & Straker, A. (1999). Chemical thinning of radiata pine. *New Zealand Journal of Forestry*, 44(1), 19–22.

- Maes, W. H., & Steppe, K. (2012). Estimating evapotranspiration and drought stress with ground-based thermal remote sensing in agriculture: A review. *Journal of Experimental Botany*, 63(13), 4671–4712. <https://doi.org/10.1093/jxb/ers165>
- Mahlein, A.-K., Rumpf, T., Welke, P., Dehne, H.-W., Plümer, L., Steiner, U., & Oerke, E.-C. (2013). Development of spectral indices for detecting and identifying plant diseases. *Remote Sensing of Environment*, 128, 21–30. <https://doi.org/10.1016/j.rse.2012.09.019>
- Martín-Benito, D., Del Río, M., Heinrich, I., Helle, G., & Cañellas, I. (2010). Response of climate-growth relationships and water use efficiency to thinning in a *Pinus nigra* afforestation. *Forest Ecology and Management*, 259(5), 967–975. <https://doi.org/10.1016/j.foreco.2009.12.001>
- McFeeters, S. K. (1996). The Use of the Normalized Difference Water Index (NDWI) in the Delineation of Open Water Features. *International Journal of Remote Sensing*, 17(7), 1425–1432. <https://doi.org/10.1080/01431169608948714>
- Merzlyak, M. N., Gitelson, A. A., Chivkunova, O. B., & Rakitin, V. Y. (1999). Non-destructive optical detection of pigment changes during leaf senescence and fruit ripening. *Physiologia Plantarum*, 106(1), 135–141. <https://doi.org/10.1034/j.1399-3054.1999.106119.x>
- Nakamura, Y., Tsujimoto, K., Ogawa, T., Noda, H. M., & Hikosaka, K. (2024). Correction of photochemical reflectance index (PRI) by optical indices to predict non-photochemical quenching (NPQ) across various species. *Remote Sensing of Environment*, 305, 114062. <https://doi.org/10.1016/j.rse.2024.114062>
- Oerke, E.-C. (2020). Remote Sensing of Diseases. *Annual Review of Phytopathology*, 58(Volume 58, 2020), 225–252. <https://doi.org/10.1146/annurev-phyto-010820-012832>
- Pan, J., Lin, J., & Xie, T. (2023). Exploring the Potential of UAV-Based Hyperspectral Imagery on Pine Wilt Disease Detection: Influence of Spatio-Temporal Scales. *Remote Sensing*, 15(9), Article 9. <https://doi.org/10.3390/rs15092281>
- Peñuelas, J., Baret, F., & Filella, I. (1995). Semi-empirical indices to assess carotenoids/chlorophyll a ratio from leaf spectral reflectance. *Photosynthetica*, 31(2), 221–230.

- Poblete, T., Camino, C., Beck, P. S. A., Hornero, A., Kattenborn, T., Saponari, M., Boscia, D., Navas-Cortes, J. A., & Zarco-Tejada, P. J. (2020). Detection of *Xylella fastidiosa* infection symptoms with airborne multispectral and thermal imagery: Assessing bandset reduction performance from hyperspectral analysis. *ISPRS Journal of Photogrammetry and Remote Sensing*, *162*, 27–40. <https://doi.org/10.1016/j.isprsjprs.2020.02.010>
- R Core Team. (2024). *R: A Language and Environment for Statistical Computing*. R Foundation for Statistical Computing. <https://www.R-project.org/>
- Riethmuller-Haage, I., Bastiaans, L., Harbinson, J., Kempenaar, C., & Kropff, M. J. (2006). Influence of the acetolactate synthase inhibitor metsulfuron-methyl on the operation, regulation and organisation of photosynthesis in *Solanum nigrum*. *Photosynthesis Research*, *88*(3), 331–341. <https://doi.org/10.1007/s11120-006-9062-z>
- Rondeaux, G., Steven, M., & Baret, F. (1996). Optimization of soil-adjusted vegetation indices. *Remote Sensing of Environment*, *55*(2), 95–107. [https://doi.org/10.1016/0034-4257\(95\)00186-7](https://doi.org/10.1016/0034-4257(95)00186-7)
- Roujean, J.-L., & Bréon, F.-M. (1995). Estimating PAR absorbed by vegetation from bidirectional reflectance measurements. *Remote Sensing of Environment*, *51*(3), 375–384. [https://doi.org/10.1016/0034-4257\(94\)00114-3](https://doi.org/10.1016/0034-4257(94)00114-3)
- Rouse, J. W., Haas, R. H., Schell, J. A., & Deering, D. W. (1974). Monitoring vegetation systems in the Great Plains with ERTS. *Third Earth Resources Technology Satellite-1 Symposium*, *1*, 309–317. <https://ntrs.nasa.gov/citations/19740022614>
- Russell, M. H., Saladini, J. L., & Lichtner, F. (2002). Sulfonylurea herbicides. *Pesticide Outlook*, *13*(4), 166–173. <https://doi.org/10.1039/b206509f>
- Sanaeifar, A., Yang, C., De La Guardia, M., Zhang, W., Li, X., & He, Y. (2023). Proximal hyperspectral sensing of abiotic stresses in plants. *Science of The Total Environment*, *861*, 160652. <https://doi.org/10.1016/j.scitotenv.2022.160652>
- Scholten, R. C., Hill, J., Werner, W., Buddenbaum, H., Dash, J. P., Gomez Gallego, M., Rolando, C. A., Pearse, G. D., Hartley, R., Estarija, H. J., & Watt, M. S. (2019). Hyperspectral VNIR-spectroscopy and imagery as a tool for monitoring herbicide damage in wilding conifers. *Biological Invasions*, *21*(11), 3395–3413. <https://doi.org/10.1007/s10530-019-02055-0>

- Sherwani, S. I., Arif, I. A., Khan, H. A., Sherwani, S. I., Arif, I. A., & Khan, H. A. (2015). Modes of Action of Different Classes of Herbicides. In *Herbicides, Physiology of Action, and Safety*. IntechOpen. <https://doi.org/10.5772/61779>
- Shibayama, M., Salli, A., Häme, T., Iso-livari, L., Heino, S., Alanen, M., Morinaga, S., Inoue, Y., & Akiyama, T. (1999). Detecting phenophases of subarctic shrub canopies by using automated reflectance measurements. *Remote Sensing of Environment*, *67*(2), 160–180. [https://doi.org/10.1016/S0034-4257\(98\)00082-0](https://doi.org/10.1016/S0034-4257(98)00082-0)
- Slaton, M. R., Raymond Hunt, E., & Smith, W. K. (2001). Estimating near-infrared leaf reflectance from leaf structural characteristics. *American Journal of Botany*, *88*(2), 278–284. <https://doi.org/10.2307/2657019>
- Smigaj, M., Agarwal, A., Bartholomeus, H., Decuyper, M., Elsherif, A., de Jonge, A., & Kooistra, L. (2023). Thermal Infrared Remote Sensing of Stress Responses in Forest Environments: A Review of Developments, Challenges, and Opportunities. *Current Forestry Reports*. <https://doi.org/10.1007/s40725-023-00207-z>
- Smigaj, M., Gaulton, R., Suárez, J. C., & Barr, S. L. (2019). Canopy temperature from an Unmanned Aerial Vehicle as an indicator of tree stress associated with red band needle blight severity. *Forest Ecology and Management*, *433*, 699–708. <https://doi.org/10.1016/j.foreco.2018.11.032>
- Still, C., Powell, R., Aubrecht, D., Kim, Y., Helliker, B., Roberts, D., Richardson, A. D., & Goulden, M. (2019). Thermal imaging in plant and ecosystem ecology: Applications and challenges. *Ecosphere*, *10*(6), e02768. <https://doi.org/10.1002/ecs2.2768>
- Traxler, C., Gaines, T. A., Küpper, A., Luemmen, P., & Dayan, F. E. (2023). The nexus between reactive oxygen species and the mechanism of action of herbicides. *The Journal of Biological Chemistry*, *299*(11), 105267. <https://doi.org/10.1016/j.jbc.2023.105267>
- Tubby, K. V., Willoughby, I. H., & Forster, J. (2017). The efficacy of chemical thinning treatments on *Pinus sylvestris* and *Larix kaempferi* and subsequent incidence and potential impact of *Heterobasidion annosum* infection in standing trees. *Forestry: An International Journal of Forest Research*, *90*(5), 728–736. <https://doi.org/10.1093/forestry/cpx038>

- Tustin, J. R. (1969). Thinning Planted Radiata Pine to Waste in State Forestry. *New Zealand Journal of Forestry*, 14(2), 210–218.
- Vapnik, V. N. (1999). *The Nature of Statistical Learning Theory*. Springer.
<https://doi.org/10.1007/978-1-4757-3264-1>
- Vogelmann, J. E., Rock, B. N., & Moss, D. M. (1993). Red edge spectral measurements from sugar maple leaves. *International Journal of Remote Sensing*, 14(8), 1563–1575.
<https://doi.org/10.1080/01431169308953986>
- Watt, M. S., Bartlett, M., Soewarto, J., de Silva, D., Estarija, H. J. C., Massam, P., Cajés, D., Yorston, W., Graevskaya, E., Dobbie, K., Fraser, S., Dungey, H. S., & Buddenbaum, H. (2023). Previsual and Early Detection of Myrtle Rust on Rose Apple Using Indices Derived from Thermal Imagery and Visible-to-Short-Infrared Spectroscopy. *Phytopathology*, 113(8), 1405–1416. <https://doi.org/10.1094/PHYTO-02-23-0078-R>
- Watt, M. S., Buddenbaum, H., Leonardo, E. M. C., Estarija, H. J., Bown, H. E., Gomez-Gallego, M., Hartley, R. J. L., Pearse, G. D., Massam, P., Wright, L., & Zarco-Tejada, P. J. (2020). Monitoring biochemical limitations to photosynthesis in N and P-limited radiata pine using plant functional traits quantified from hyperspectral imagery. *Remote Sensing of Environment*, 248, 112003. <https://doi.org/10.1016/j.rse.2020.112003>
- Watt, M. S., Estarija, H. J. C., Bartlett, M., Main, R., Pasquini, D., Yorston, W., McLay, E., Zhulanov, M., Dobbie, K., Wardhaugh, K., Hossain, Z., Fraser, S., & Buddenbaum, H. (2024). Early Detection of Myrtle Rust on Pōhutukawa Using Indices Derived from Hyperspectral and Thermal Imagery. *Remote Sensing*, 16(6), Article 6.
<https://doi.org/10.3390/rs16061050>
- Watt, M. S., Leonardo, E. M. C., Estarija, H. J. C., Massam, P., de Silva, D., O'Neill, R., Lane, D., McDougal, R., Buddenbaum, H., & Zarco-Tejada, P. J. (2021). Long-term effects of water stress on hyperspectral remote sensing indicators in young radiata pine. *Forest Ecology and Management*, 502, 119707. <https://doi.org/10.1016/j.foreco.2021.119707>
- Watt, M. S., Pearse, G. D., Dash, J. P., Melia, N., & Leonardo, E. M. C. (2019). Application of remote sensing technologies to identify impacts of nutritional deficiencies on forests. *ISPRS*

Journal of Photogrammetry and Remote Sensing, 149, 226–241.

<https://doi.org/10.1016/j.isprsjprs.2019.01.009>

- Watt, M. S., Poblete, T., De Silva, D., Estarija, H. J. C., Hartley, R. J. L., Leonardo, E. M. C., Massam, P., Buddenbaum, H., & Zarco-Tejada, P. J. (2023). Prediction of the severity of Dothistroma needle blight in radiata pine using plant based traits and narrow band indices derived from UAV hyperspectral imagery. *Agricultural and Forest Meteorology*, 330, 109294. <https://doi.org/10.1016/j.agrformet.2022.109294>
- Willoughby, I. H., Stokes, V. J., & Connolly, T. (2017). Using Ecoplugs containing glyphosate can be an effective method of killing standing trees. *Forestry: An International Journal of Forest Research*, 90(5), 719–727. <https://doi.org/10.1093/forestry/cpx028>
- Wu, C., Niu, Z., Tang, Q., & Huang, W. (2008). Estimating chlorophyll content from hyperspectral vegetation indices: Modeling and validation. *Agricultural and Forest Meteorology*, 148(8–9), 1230–1241. <https://doi.org/10.1016/j.agrformet.2008.03.005>
- Wu, W., Zhang, Z., Zheng, L., Han, C., Wang, X., Xu, J., & Wang, X. (2020). Research Progress on the Early Monitoring of Pine Wilt Disease Using Hyperspectral Techniques. *Sensors (Basel, Switzerland)*, 20(13), 3729. <https://doi.org/10.3390/s20133729>
- Yu, R., Luo, Y., & Ren, L. (2024). Detection of pine wood nematode infestation using hyperspectral drone images. *Ecological Indicators*, 162, 112034. <https://doi.org/10.1016/j.ecolind.2024.112034>
- Zarco-Tejada, P. J., Berjón, A., Lopez-Lozano, R., Miller, J. R., Martín, P., Cachorro, V., González, M. R., & de Frutos, A. (2005). Assessing vineyard condition with hyperspectral indices: Leaf and canopy reflectance simulation in a row-structured discontinuous canopy. *Remote Sensing of Environment*, 99(3), 271–287. <https://doi.org/10.1016/j.rse.2005.09.002>
- Zarco-Tejada, P. J., Camino, C., Beck, P. S. A., Calderon, R., Hornero, A., Hernández-Clemente, R., Kattenborn, T., Montes-Borrego, M., Susca, L., Morelli, M., Gonzalez-Dugo, V., North, P. R. J., Landa, B. B., Boscia, D., Saponari, M., & Navas-Cortes, J. A. (2018). Previsual symptoms of *Xylella fastidiosa* infection revealed in spectral plant-trait alterations. *Nature Plants*, 4(7), Article 7. <https://doi.org/10.1038/s41477-018-0189-7>

- Zarco-Tejada, P. J., González-Dugo, V., & Berni, J. A. J. (2012). Fluorescence, temperature and narrow-band indices acquired from a UAV platform for water stress detection using a micro-hyperspectral imager and a thermal camera. *Remote Sensing of Environment*, 117, 322–337. <https://doi.org/10.1016/j.rse.2011.10.007>
- Zarco-Tejada, P. J., Miller, J. R., Mohammed, G. H., & Noland, T. L. (2000). Chlorophyll Fluorescence Effects on Vegetation Apparent Reflectance: I. Leaf-Level Measurements and Model Simulation. *Remote Sensing of Environment*, 74(3), 582–595. [https://doi.org/10.1016/S0034-4257\(00\)00148-6](https://doi.org/10.1016/S0034-4257(00)00148-6)
- Zarco-Tejada, P. J., Miller, J. R., Noland, T. L., Mohammed, G. H., & Sampson, P. H. (2001). Scaling-up and model inversion methods with narrowband optical indices for chlorophyll content estimation in closed forest canopies with hyperspectral data. *IEEE Transactions on Geoscience and Remote Sensing*, 39(7), 1491–1507. <https://doi.org/10.1109/36.934080>
- Zarco-Tejada, P. J., Morales, A., Testi, L., & Villalobos, F. J. (2013). Spatio-temporal patterns of chlorophyll fluorescence and physiological and structural indices acquired from hyperspectral imagery as compared with carbon fluxes measured with eddy covariance. *Remote Sensing of Environment*, 133, 102–115. <https://doi.org/10.1016/j.rse.2013.02.003>
- Zhang, N., Yang, G., Pan, Y., Yang, X., Chen, L., & Zhao, C. (2020). A Review of Advanced Technologies and Development for Hyperspectral-Based Plant Disease Detection in the Past Three Decades. *Remote Sensing*, 12(19), Article 19. <https://doi.org/10.3390/rs12193188>

APPENDICES

Table A1. List of hyperspectral and multispectral indices and their formulations used in the study.

Indices	Index code	Equation	Reference
<u>Hyperspectral Indices</u>			
Structural indices			
Enhanced Vegetation Index	EVI	$2.5 \cdot (R_{800} - R_{670}) / (R_{800} + 6 \cdot R_{670} - 7.5 \cdot R_{800} + 1)$	(Liu & Huete, 1995)
Modified Chlorophyll Abs. Index	MCARI	$[(R_{700} - R_{670}) - 0.2(R_{700} - R_{550})] \cdot (R_{700}/R_{670})$	(Daughtry et al., 2000)
Modified Chlorophyll Abs. Index 1	MCARI1	$1.2 \cdot [(2.5 \cdot (R_{800} - R_{670})) - (1.3 \cdot (R_{800} - R_{550}))]$	(C. Wu et al., 2008)
Modified Simple Ratio	MSR	$\frac{R_{800}/R_{670} - 1}{(R_{800}/R_{670})^{0.5} + 1}$	(Chen, 1996)
Modified Triangular Veg. Index 1	MTVI1	$1.2[1.2(R_{800} - R_{550}) - 2.5(R_{670} - R_{550})]$	(Haboudane et al., 2004)
Normalized Difference Veg. Index	NDVI	$(R_{800} - R_{670}) / (R_{800} + R_{670})$	(Rouse et al., 1974)
Optimized Soil-Adjusted Veg. Index	OSAVI	$((1 + 0.16) \cdot (R_{800} - R_{670}) / (R_{800} + R_{670} + 0.16))$	(Rondeaux et al., 1996)
Renormalized Difference Veg. Index	RDVI	$(R_{800} - R_{670}) / \sqrt{(R_{800} + R_{670})}$	(Roujean & Bréon, 1995)
Simple Ratio	SR	R_{800}/R_{670}	(Jordan, 1969)
Triangular Vegetation Index	TVI	$0.5 \cdot [120 \cdot (R_{750} - R_{550}) - 200 \cdot (R_{670} - R_{550})]$	(Broge & Leblanc, 2001)
Pigment indices			
Carter Index	CAR	R_{695}/R_{760}	(Carter et al., 1996)
Chlorophyll Index Red Edge	CI	R_{750}/R_{710}	(Zarco-Tejada et al., 2001)
Modified Carotenoid Reflectance Index	mCRI	$\left[\left(\frac{1}{R_{510}} \right) - \left(\frac{1}{R_{550}} \right) \right] R_{780}$	(Gitelson et al., 2002)
Carotenoid Reflectance Indices	CRI550	$(1/R_{510}) - (1/R_{550})$	(Gitelson et al., 2003, 2006)
Carotenoid Reflectance Indices	CRI550_515	$(1/R_{515}) - (1/R_{550})$	(Gitelson et al., 2006)
Carotenoid Reflectance Indices	CRI700	$(1/R_{510}) - (1/R_{700})$	(Gitelson et al., 2003, 2006)
Carotenoid Reflectance Indices	CRI700_515	$(1/R_{515}) - (1/R_{700})$	(Gitelson et al., 2006)
Reflectance band ratio indices	DCab	$R_{672}/(R_{550} \cdot 3R_{708})$	(Datt, 1998)
Reflectance band ratio indices	DNIRCab	$R_{860}/(R_{550} \cdot R_{708})$	(Datt, 1998)
Gitelson & Merzlyak index 1	GM1	R_{750}/R_{550}	(Gitelson & Merzlyak, 1997)
Gitelson & Merzlyak index 2	GM2	R_{750}/R_{700}	(Gitelson & Merzlyak, 1997)
Pigment Specific Normalized Difference a	PSNDa	$(R_{800} - R_{675}) / ((R_{800} + R_{675}))$	(Blackburn, 1998)

Pigment Specific Normalized Difference b635	PSNDb(635)	$(R_{800} - R_{635}) / ((R_{800} + R_{635}))$	(Blackburn, 1998)
Pigment Specific Normalized Difference b650	PSNDb(650)	$(R_{800} - R_{650}) / ((R_{800} + R_{650}))$	(Blackburn, 1998)
Pigment Specific Normalized Difference c	PSNDc	$(R_{800} - R_{470}) / (R_{800} + R_{470})$	(Blackburn, 1998)
Plant Senescence Reflectance Index	PSRI	$(R_{680} - R_{500}) / R_{750}$	(Merzlyak et al., 1999)
Pigment Specific Simple Ratio Chlorophyll a	PSSR_a	R_{800} / R_{675}	(Blackburn, 1998)
Pigment Specific Simple Ratio Carotenoids c	PSSR_c	R_{800} / R_{500}	(Blackburn, 1998)
Carotenoid Reflectance Index	RNIR_CRI550	$(1/R_{510}) - (1/R_{550}) \cdot R_{770}$	(Gitelson et al., 2003, 2006)
Carotenoid Reflectance Index	RNIR_CRI700	$(1/R_{510}) - (1/R_{700}) \cdot R_{770}$	(Gitelson et al., 2003, 2006)
Structure-Intensive Pigment Index	SIPI	$(R_{800} - R_{445}) / (R_{800} + R_{680})$	(Peñuelas et al., 1995)
Transformed Chlorophyll Absorption in Reflectance Index	TCARI	$3 \cdot [(R_{700} - R_{670}) - 0.2 \cdot (R_{700} - R_{550}) \cdot (R_{700}/R_{670})]$	(Haboudane et al., 2002)
Transformed Chlorophyll Absorption in Reflectance Index/ Optimized Soil-Adjusted Vegetation Index	TCARI_OSAVI	$\frac{3 \cdot [(R_{700} - R_{670}) - 0.2 \cdot (R_{700} - R_{550}) \cdot (R_{700}/R_{670})]}{((1 + 0.16) \cdot (R_{800} - R_{670}) / (R_{800} + R_{670} + 0.16))}$	(Haboudane et al., 2002)
Vogelmann indices	VOG	R_{740} / R_{720}	(Vogelmann et al., 1993)
Vogelmann indices	VOG2	$(R_{734} - R_{747}) / (R_{715} + R_{726})$	(Vogelmann et al., 1993)
Vogelmann indices	VOG3	$(R_{734} - R_{747}) / (R_{715} + R_{720})$	(Vogelmann et al., 1993)
Simple Ratio	SR510_770	R_{510} / R_{770}	(Nakamura et al., 2024)
Simple Ratio	SR510_574	R_{510} / R_{574}	(Nakamura et al., 2024)
Simple Ratio	SR528_574	R_{528} / R_{574}	(Nakamura et al., 2024)
Simple Ratio	SR800_635	R_{800} / R_{635}	(Nakamura et al., 2024)
Normalized Difference	ND636_770	$(R_{636} - R_{770}) / ((R_{636} + R_{770}))$	(Nakamura et al., 2024)
Normalized Pigments Index	NPCI	$(R_{680} - R_{430}) / (R_{680} + R_{430})$	(Peñuelas et al., 1995)
Reflectance Curvature Index	CUR	$(R_{675} \cdot R_{690}) / R_{683}^2$	(Zarco-Tejada et al., 2000)
Carotenoid/Chlorophyll Ratio Index	PRICI	$(R_{570} - R_{530}) / (R_{570} + R_{530}) \cdot ((R_{760}/R_{700}) - 1)$	(Garrity et al., 2011)
Photochemical Refl. Index (515)	PRI515	$(R_{515} - R_{531}) / (R_{515} + R_{531})$	(Hernández-Clemente et al., 2011)
Photochemical Refl. Index (570)	PRI570	$(R_{570} - R_{531}) / (R_{570} + R_{531})$	(Gamon et al., 1992)
Photochemical Refl. Index (512)	PRIm1	$(R_{512} - R_{531}) / (R_{512} + R_{531})$	(Hernández-Clemente et al., 2011)
Photochemical Refl. Index (600)	PRIm2	$(R_{600} - R_{531}) / (R_{600} + R_{531})$	(Gamon et al., 1992)
Photochemical Refl. Index (670)	PRIm3	$(R_{670} - R_{531}) / (R_{670} + R_{531})$	(Gamon et al., 1992)
Photochemical Refl. Index (670 and 570)	PRIm4	$(R_{570} - R_{531} - R_{670}) / (R_{570} + R_{531} + R_{670})$	(Hernández-Clemente et al., 2011)
Normalized Photoch. Refl. Index	PRIn	$PRI_{570} / [RDVI \cdot (R_{700}/R_{670})]$	(Zarco-Tejada et al., 2013)
Normalized Difference	ND510_770	$(R_{510} - R_{770}) / ((R_{510} + R_{770}))$	(Nakamura et al., 2024)

R/G/B indices

Blue Index	B	R_{450}/R_{490}	(Calderón et al., 2013)
Blue/green index	BGI	R_{450}/R_{550}	(Zarco-Tejada et al., 2005)
Blue/red index	BRI	R_{450}/R_{690}	(Zarco-Tejada et al., 2012)
Greenness Index	G	R_{570}/R_{670}	(Calderón et al., 2013)
Lichtenthaler Index 1	LIC1	$(R_{800} - R_{680})/(R_{800} + R_{680})$	(Lichtenthaler, 1996)
Lichtenthaler Index 2	LIC2	R_{440}/R_{690}	(Lichtenthaler, 1996)
Lichtenthaler Index 3	LIC3	R_{440}/R_{740}	(Lichtenthaler, 1996)
Lichtenthaler Index 4	LIC4	R_{440}/R_{520}	(Lichtenthaler, 1996)
Lichtenthaler Index 5	LIC5	R_{690}/R_{520}	(Lichtenthaler, 1996)
Lichtenthaler Index 6	LIC6	R_{740}/R_{520}	(Lichtenthaler, 1996)
Lichtenthaler Index 7	LIC7	R_{690}/R_{740}	(Lichtenthaler, 1996)
Redness Index	R	R_{700}/R_{670}	(Gitelson et al., 2000)
Ratio Analysis of Reflectance Spectra	RARS	R_{746}/R_{513}	(Chappelle et al., 1992)
Red/green indices	RGI	R_{690}/R_{550}	(Zarco-Tejada et al., 2005)

Plant disease indices

Healthy-index	HI	$\frac{R_{534} - R_{698}}{R_{534} + R_{698}} - \frac{1}{2} \cdot R_{704}$	(Mahlein et al., 2013)
---------------	----	---	------------------------

Multispectral indices

Normalized Difference Vegetation Index	NDVI	$(NIR - Red)/(NIR + Red)$	(Rouse et al., 1974)
Normalized Difference Vegetation Index	NDVI2	$(NIR - Red2)/(NIR + Red2)$	(Lad et al., 2023)
Green Normalized Difference Vegetation Index	GNDVI	$(NIR - Green)/(NIR + Green)$	(Gitelson & Merzlyak, 1997)
Green Normalized Difference Vegetation Index	GNDVI2	$(NIR - Green2)/(NIR + Green2)$	(Gitelson & Merzlyak, 1997)
Normalized Difference Red Edge	NDRE	$(NIR - Red\ Edge1)/(NIR + Red\ Edge1)$	(Filella & Peñuelas, 1994)
Green Ratio Vegetation Index	GRVI	$NIR/ Green$	(Shibayama et al., 1999)
Normalized Difference Water Index	NDWI	$(Green - NIR)/(Green + NIR)$	(McFeeters, 1996)
Physiological Reflectance Index	PRI	$(Green2 - Green)/(Green2 + Green)$	(Gamon et al., 1997)
Foliar Moisture Content Index	FMCI	$(Red\ Edge3 - NIR)/(Red\ Edge3 + NIR)$	(Lad et al., 2023)

Table A2. Results of *t*-tests comparing multispectral index values between *crop* and *cull* treatments per timepoint. The *p* values are color-coded according to the strength of the significance. Gold shaded cells indicate $p < 0.001$, green cells indicate $p < 0.01$, and blue indicates $p < 0.05$. Indices are ordered by increasing mean *p*-value, calculated using the six treated blocks, from 13 days after treatment (DAT) to 47 DAT.

Index	Control	13 DAT	18 DAT	27 DAT	32 DAT	41 DAT	47 DAT
PRI	0.859	0.024	0.000	0.000	0.000	0.000	0.000
NDVI2	0.958	0.255	0.039	0.000	0.000	0.000	0.000
NDVI	0.845	0.317	0.053	0.000	0.000	0.000	0.000
GNDVI	0.745	0.312	0.114	0.000	0.002	0.000	0.000
NDWI	0.745	0.312	0.114	0.000	0.002	0.000	0.000
NDRE	0.863	0.361	0.104	0.000	0.001	0.000	0.000
GNDVI2	0.740	0.372	0.199	0.000	0.005	0.000	0.000
GRVI	0.521	0.581	0.439	0.195	0.002	0.000	0.000
RE	0.887	0.995	0.317	0.019	0.000	0.000	0.000
FMCi	0.544	0.900	0.804	0.190	0.982	0.004	0.000

Table A3. Results of *t*-tests comparing hyperspectral index values between *crop* and *cull* treatments per timepoint. The p values are color-coded according to the strength of the significance. Gold shaded cells indicate $p < 0.001$, green cells indicate $p < 0.01$, and blue indicates $p < 0.05$. Indices are ordered within their category by increasing mean p-value calculated using all six treated blocks, from 13 days after treatment (DAT) to 47 DAT, while their overall rank across all categories is also given.

Category	Index	Control	13 DAT	18 DAT	27 DAT	32 DAT	41 DAT	47 DAT	Rank
Disease	HI	0.093	0.043	0.008	0.000	0.000	0.000	0.000	5
Pigment	PRICI	0.244	0.009	0.004	0.000	0.000	0.000	0.000	1
	PRIn	0.644	0.009	0.005	0.000	0.000	0.000	0.000	2
	PRI570	0.144	0.019	0.003	0.000	0.000	0.000	0.000	3
	SR528_574	0.384	0.030	0.000	0.000	0.000	0.000	0.000	4
	PSRI	0.012	0.070	0.013	0.000	0.000	0.000	0.000	6
	CAR	0.197	0.056	0.056	0.000	0.000	0.000	0.000	7
	ND636_770	0.231	0.086	0.050	0.000	0.000	0.000	0.000	10
	PSNDb635	0.230	0.082	0.058	0.000	0.000	0.000	0.000	11
	PRIm2	0.115	0.111	0.031	0.000	0.000	0.000	0.000	12
	PSNDb650	0.176	0.091	0.068	0.000	0.000	0.000	0.000	13
	VOG	0.780	0.040	0.128	0.000	0.000	0.000	0.000	16
	NPCI	0.057	0.128	0.070	0.000	0.000	0.000	0.000	20
	PSNDa	0.130	0.101	0.113	0.000	0.000	0.000	0.000	22
	SR510_574	0.307	0.107	0.002	0.014	0.117	0.000	0.000	25
	CI	0.808	0.045	0.202	0.000	0.000	0.000	0.000	26
	VOG2	0.829	0.033	0.251	0.000	0.000	0.000	0.000	28
	GM2	0.702	0.057	0.241	0.000	0.000	0.000	0.000	29
	VOG3	0.851	0.035	0.267	0.000	0.000	0.000	0.000	30
	SIPI	0.223	0.114	0.190	0.000	0.000	0.000	0.000	31
	PRIm3	0.019	0.262	0.117	0.000	0.000	0.000	0.000	33
	SR510_769	0.344	0.130	0.301	0.000	0.000	0.000	0.000	34
	SR800_635	0.666	0.101	0.336	0.000	0.000	0.000	0.000	35
	ND510_770	0.352	0.131	0.308	0.000	0.000	0.000	0.000	36
	GM1	0.743	0.084	0.368	0.000	0.001	0.000	0.000	37
	PSSRa	0.511	0.121	0.359	0.000	0.000	0.000	0.000	38
	PSNDc	0.403	0.208	0.653	0.000	0.000	0.000	0.000	43
	PSSRc	0.692	0.180	0.894	0.000	0.000	0.000	0.000	46
	mCRI	0.668	0.225	0.862	0.000	0.000	0.000	0.000	47
	RNIR_CRI550	0.642	0.253	0.867	0.000	0.000	0.000	0.000	48
	RNIR_CRI700	0.659	0.338	0.876	0.000	0.001	0.000	0.000	49
	TCA_OSA	0.437	0.287	0.500	0.000	0.480	0.000	0.001	50
	PRI515	0.401	0.758	0.771	0.000	0.000	0.000	0.000	53
	PRIm4	0.038	0.893	0.668	0.001	0.000	0.000	0.000	54
	DCab	0.235	0.607	0.478	0.453	0.003	0.062	0.000	55
	PRIm1	0.285	0.910	0.730	0.000	0.000	0.000	0.000	57
	CRI700	0.275	0.918	0.226	0.003	0.263	0.024	0.256	58
	DNIRCab	0.304	0.252	0.703	0.000	0.905	0.000	0.000	60
	CRI550_515	0.283	0.989	0.405	0.000	0.762	0.000	0.000	61
	CRI550	0.286	0.951	0.354	0.000	0.877	0.000	0.000	62
	CRI700_515	0.270	0.852	0.234	0.010	0.156	0.089	0.875	63
	TCARI	0.429	0.655	0.952	0.013	0.369	0.012	0.592	65
	CUR	0.058	0.989	0.624	0.573	0.494	0.003	0.000	66
R/G/B	BRI	0.060	0.058	0.066	0.000	0.000	0.000	0.000	8
	LIC5	0.011	0.095	0.033	0.000	0.000	0.000	0.000	9

LIC7	0.141	0.092	0.072	0.000	0.000	0.000	0.000	14
LIC2	0.147	0.082	0.097	0.000	0.000	0.000	0.000	17
LIC1	0.155	0.096	0.107	0.000	0.000	0.000	0.000	21
RGI	0.030	0.218	0.097	0.000	0.000	0.000	0.000	32
LIC6	0.744	0.160	0.477	0.000	0.000	0.000	0.000	40
RARS	0.614	0.150	0.507	0.000	0.000	0.000	0.000	41
G	0.036	0.465	0.364	0.000	0.000	0.000	0.000	42
LIC3	0.490	0.365	0.557	0.000	0.000	0.000	0.000	44
LIC4	0.989	0.270	0.417	0.003	0.216	0.001	0.036	45
BGI	0.992	0.245	0.219	0.439	0.046	0.177	0.185	51
B	0.116	0.273	0.410	0.000	0.699	0.000	0.000	52
R	0.034	0.966	0.786	0.000	0.000	0.000	0.000	59
Structural								
RDVI	0.986	0.119	0.048	0.000	0.000	0.000	0.000	15
OSAVI	0.762	0.131	0.055	0.000	0.000	0.000	0.000	18
NDVI	0.126	0.096	0.100	0.000	0.000	0.000	0.000	19
MCARI1	0.619	0.168	0.059	0.001	0.000	0.001	0.000	23
MTVI1	0.619	0.168	0.059	0.001	0.000	0.001	0.000	24
TVI	0.582	0.215	0.052	0.002	0.000	0.001	0.000	27
SR	0.457	0.143	0.438	0.000	0.000	0.000	0.000	39
MSR	0.044	0.872	0.756	0.000	0.000	0.000	0.000	56
MCARI	0.746	0.575	0.859	0.398	0.060	0.328	0.014	64
EVI	0.803	0.738	0.146	0.115	0.225	0.964	0.686	67